bioRxiv preprint doi: https://doi.org/10.1101/2020.12.31.424978; this version posted January 1, 2021. The copyright holder for this preprint (which was not certified by peer review) is the author/funder, who has granted bioRxiv a license to display the preprint in perpetuity. It is made available under aCC-BY-NC-ND 4.0 International license.

Bulkhead-like apical membrane structures between hepatocytes are required for anisotropic lumen expansion and liver tissue morphogenesis

Lenka Belicova[1], Urska Repnik[1,2], Julien Delpierre[1], Elzbieta Gralinska[3], Sarah Seifert[1], José Ignacio Valenzuela[1], Hernán Andrés Morales-Navarrete[1], Christian Franke[1,6], Helin Räägel[1,7], Evgeniya Shcherbinina[4], Tatiana Prikazchikova[4], Victor Koteliansky[4] , Martin Vingron[3], Yannis Kalaidzidis[1], Timofei Zatsepin[4,5] and Marino Zerial[1, 8,*]

Affiliations

[1]Max Planck Institute of Molecular Cell Biology and Genetics, 01307 Dresden, Germany.
[2]Present address: Zentrale Mikroskopie im Biologiezentrum der Christian-Albrechts-Universität zu Kiel, 24118 Kiel, Germany.
[3]Department of Computational Molecular Biology, Max Planck Institute for Molecular Genetics, 14195 Berlin, Germany.
[4]Skolkovo Institute of Science and Technology, Skolkovo, Russia.
[5]Lomonosov Moscow State University, Department of Chemistry, Moscow, 119991, Russia.
[6] Present address: Institute of Applied Optics and Biophysics, Friedrich-Schiller-University Jena, Max-Wien Platz 4, 07743 Jena, Germany.
[7]Nelson Laboratories LLC, Salt Lake City, Utah 84123, United States.
[8]Lead contact
[*]Correspondence: zerial@mpi-cbg.de

Summary

Cell polarity is key to epithelial organization. Whereas polarized epithelial cells have a single apico-basal axis, hepatocytes exhibit a complex multi-axial polarity. During development, the apical surfaces of hepatocytes elongate anisotropically, generating a 3D tubular network of bile canaliculi (BC). Here, to elucidate the mechanisms of hepatocyte polarity and re-engineer it into simple epithelial polarity, we optimised a culture system of primary mouse hepatoblasts that recapitulates hepatocyte differentiation and BC morphogenesis. Remarkably, we discovered a pattern of specific extensions of the apical membrane sealed by tight junctions traversing the lumen between two adjacent hepatocytes that remind the bulkheads of boats. These apical bulkheads were observed also in the developing liver. Screening for molecular factors required for hepatocyte polarity revealed that silencing of Rab35 caused loss of the bulkheads, conversion into simple polarity, formation of cyst-like structures and change in cell fate. By

bioRxiv preprint doi: https://doi.org/10.1101/2020.12.31.424978; this version posted January 1, 2021. The copyright holder for this preprint (which was not certified by peer review) is the author/funder, who has granted bioRxiv a license to display the preprint in perpetuity. It is made available under aCC-BY-NC-ND 4.0 International license.

exploiting Rab35 depletion in the developing liver we could re-engineer hepatocyte polarity and trigger formation of epithelial tubes. Our results suggest a new model of BC morphogenesis based on mechanical stabilization of the tubular lumen.

Introduction

Epithelial tubes are essential components of several organs, such as kidney and intestine. They are composed of cells that exhibit apico-basal polarity, with the apical surface facing the internal *lumen* and the basal surface contacting the basement membrane (Andrew and Ewald, 2010; Bryant and Mostov, 2008). The liver contains two types of epithelial cells, bile duct cells (cholangiocytes) and hepatocytes, both derived from embryonic progenitors called hepatoblasts (Müsch, 2018). Bile duct cells are cuboidal or columnar epithelial cells with the typical apico-basal polarity and the apical surfaces sharing a common lumen (Boyer, 2013; Treyer & Müsch, 2013). Hepatocytes, the most abundant epithelial cells of the liver parenchyma, have a specialized polarity which cannot be described using only one apico-basal axis as in simple epithelia (Treyer & Müsch, 2013). Hepatocytes are multi-polar with bi-axial polarity characterized by two nematic axes (Morales-Navarrete et al., 2019). *In vivo,* each hepatocyte faces the sinusoidal endothelium via multiple basal domains and can initiate apical *lumina* with several neighbouring hepatocytes. In the developing liver, hepatocyte lumina anisotropically elongate as a tubular belt surrounding the cells, intersecting the contact membranes between two neighbouring hepatocytes (lateral domain). The lumina eventually interconnect to create a complex 3D luminal network of highly ramified ~ 1 µm-thin bile canaliculi (BC) (Morales-Navarrete et al., 2015). The function of BC is to transport the bile secreted from the apical surface of the hepatocytes towards the bile ducts. Bile flow through BC is supported by the osmotic pressure but also by a significant contribution of acto-myosin-dependent contractility (Meyer et al., 2017; Watanabe et al., 1991). However, the fact that such contractility does not appear to yield peristaltic movements is puzzling and calls for a mechanistic explanation.

Liver tissue organization and function therefore depends on the generation of simple epithelial polarity vs. hepatocyte polarity and their resulting lumen morphologies, whose

bioRxiv preprint doi: https://doi.org/10.1101/2020.12.31.424978; this version posted January 1, 2021. The copyright holder for this preprint (which was not certified by peer review) is the author/funder, who has granted bioRxiv a license to display the preprint in perpetuity. It is made available under aCC-BY-NC-ND 4.0 International license.

mechanisms are not fully understood (Gissen and Arias, 2015; Müsch, 2014, 2018; Ober and Lemaigre, 2018; Tanimizu and Mitaka, 2017). In 3D *in vitro* cultures, bile duct cells form spherical cysts with a hollow lumen, similar to the well-studied MDCK cell system (O'Brien et al., 2002; Tanimizu et al., 2007). Hepatocytes, on the other hand, can polarize and form BC-like structures *in vitro* (Fu et al., 2010; Zeigerer et al., 2017). Interestingly, overexpression of Par1b in MDCK cells altered the spindle orientation and resulted in the reorganization of the lumina such that they resembled that of hepatocytes. Conversely, Par1b down-regulation in hepatocyte cell lines (HepG2 and WIF9B) re-oriented the microtubules as in epithelial cells, leading to simple apico-basal polarity (Cohen et al., 2004b, 2004a; Lázaro-Diéguez et al., 2013; Slim et al., 2013). However, these studies were conducted on hepatocyte cell lines which do not recapitulate the peculiar elongated tubular morphology of BC, but rather form lateral spherical lumina (Cohen et al., 2004b; de Marco et al., 2002). The mechanisms underlying the morphogenesis of the elongated and branched morphology of BC still remain elusive (Fu et al., 2010, 2011; Li et al., 2016).

In early development (E13-14 in mouse and rat), clusters of hepatocytes generate small separate spherical lumina that eventually interconnect into a continuous network, concomitant with hematopoietic progenitors leaving the liver (E17-21) (Ober and Lemaigre, 2018; Tanimizu and Mitaka, 2016; Treyer and Müsch, 2013). Based on *in vitro* studies using hepatocyte cell lines or primary hepatocytes, Tanimizu and Mitaka (2017) argued for a model where cell division is a key determinant of apical lumen elongation. According to this model, actively proliferating foetal hepatocytes change the mode of cell division. In the first stage, hepatocytes divide asymmetrically and form different lumina with neighbouring hepatocytes (Overeem et al., 2015). If cell division is symmetric, e.g. upon Par1b depletion, cells share the same lumen by forming a cyst (Slim et al., 2013). In the second stage, hepatocytes orient their spindle orthogonal to the lumen axis and undergo an incomplete division that prevents lumen partitioning between two daughter cells, thus leading the initial spherical lumen to elongate into a typical BC tubule (Tanimizu and Mitaka, 2017; Wang et al., 2014). In the developing liver however, as hepatoblasts differentiate into hepatocytes, they gradually stop proliferating, declining from 25% dividing at E14.5 to mostly quiescent at E17.5 (Yang et al., 2017). Yet,

bioRxiv preprint doi: https://doi.org/10.1101/2020.12.31.424978; this version posted January 1, 2021. The copyright holder for this preprint (which was not certified by peer review) is the author/funder, who has granted bioRxiv a license to display the preprint in perpetuity. It is made available under aCC-BY-NC-ND 4.0 International license.

between E14.5 and E17.5, the small isolated apical lumina expand and generate an almost fully connected BC network (Tanimizu et al., 2016; see below Fig. 7C). This means that foetal hepatocytes require additional mechanisms independent of cell division to elongate BC that could not be captured in cell lines or mature hepatocyte model systems.

We can envisage a model where a lumen elongates via anisotropic tension of the apical plasma membrane. The tubular structures in other systems, such as for example the Drosophila tracheal tube, possess a periodic supra-cellular actin pattern (Hannezo et al., 2015; Hayashi and Dong, 2017) that could help stabilizing hepatocyte lumina as they elongate and prevent an isotropic expansion. Up to date, there is only little understanding of the generation and elongation of hepatocyte apical lumina (Li et al., 2016; Müsch, 2018; Ober and Lemaigre, 2018; Tanimizu and Mitaka, 2017).

In this study, we used cultures of primary mouse hepatoblasts to elucidate the mechanisms underlying the anisotropic expansion of the apical lumen for BC formation. We succeeded in re-engineering the polarity of hepatocytes and converting it into the polarity of simple epithelial cells, generating epithelial tubes instead of BC in the developing embryonic liver.

Results

Lumen morphogenesis in hepatocytes is accompanied by specific actin structures that interconnect the two lumen-forming cells

To understand how hepatocytes polarize to form apical lumina of tubular shape, we took advantage of a well-established culture of primary mouse hepatoblasts isolated from embryonic livers based on Dlk expression (Tanimizu et al., 2003), but optimized the conditions (Methods) to differentiate them into hepatocytes and generate BC *in vitro* (Figure 1A). The hepatoblasts formed elongated and branched tubular lumina enriched in F-actin, and positive for the apical marker CD13 and the tight junction protein ZO-1 (Figure 1B). This system therefore recapitulates the formation of branched BC-lumina *in vitro* similar to the developing liver *in vivo*. The differentiation to hepatocytes was confirmed by gene expression profiling. We

bioRxiv preprint doi: https://doi.org/10.1101/2020.12.31.424978; this version posted January 1, 2021. The copyright holder for this preprint (which was not certified by peer review) is the author/funder, who has granted bioRxiv a license to display the preprint in perpetuity. It is made available under aCC-BY-NC-ND 4.0 International license.

used RNA-seq to compare isolated hepatoblasts, *in vitro* differentiated hepatocytes and mature hepatocytes isolated from adult livers as control. *In vitro* differentiated hepatocytes down-regulated the hepatoblast marker *Dlk* and up-regulated genes expressed in mature hepatocytes, e.g. metabolic genes such as *Tat, G6pc, Pck1, Cyp3a11* (Figure 1C).

To study lumen morphogenesis, we performed live-cell time-lapse microscopy on differentiating hepatoblasts stably expressing LifeAct-EGFP as actin label. We followed lumenogenesis for up to 52 hours in 10 minute intervals and categorised four sequential steps: 1) lumen initiation, 2) elongation, 3) branching and 4) fusion. We frequently observed single cells initiating multiple individual lumina with their neighbours (Figure S1A, Video Figure S1A). Interestingly, such multiplicity of lumina formed independently of cell division. This is a general phenomenon because dividing cells were rarely observed. After formation, lumina elongated into tubes until they spanned the entire cell–cell contact (Figure 1D, S1A, S1B, S1C, Videos Figure 1D, S1A, S1B, S1C). At this point, a lumen could fuse with another lumen (Figure S1B, left panels) branching at a 3-cell contact (Figure S1B, right panels).

The elongation of lumina in the absence of cell division implies the existence of anisotropic forces. Interestingly, we also observed instances when the lumina transiently acquired a rounded shape (Figure 1D, Figure S1C, Videos Figure 1D, S1C) but these structures did not expand isotropically to form a spherical lumen. They were subsequently “corrected”, suggesting the existence of control mechanisms which actively enforce anisotropy to prevent the formation of cyst-like structures typical of epithelial cells (Bryant and Mostov, 2008).

We were intrigued by the presence of dark stripes in the bright-field, transverse to the direction of lumen elongation (e.g. Figure 1D, S1) which may correspond to high curvature of the apical membranes. The stripes also coincided with areas of high density of actin (LifeAct-EGFP) and gave the impression to originate mainly from one cell. We will see below that this asymmetry of stripes is most likely due to mismatch orientation of focal plane vs. convoluted cell-cell contacts. The pattern was evident early in lumen formation and continued as the lumina elongated, keeping a characteristic spacing between stripes (Figure 1D, S1). Interestingly, when the lumen bulged outward, for example in Figure 1D’ (marked with a star),

bioRxiv preprint doi: https://doi.org/10.1101/2020.12.31.424978; this version posted January 1, 2021. The copyright holder for this preprint (which was not certified by peer review) is the author/funder, who has granted bioRxiv a license to display the preprint in perpetuity. It is made available under aCC-BY-NC-ND 4.0 International license.

tending to a spherical lumen, it coincided with the loss of the stripes. Subsequently, the tubular shape of the lumen recovered once additional stripes formed, suggesting an active link between the striped pattern and the anisotropy of lumen elongation.

To determine the micro-structure of the actin-rich stripes, we analysed the cortical F-actin labelled with Phalloidin-Alexa-647 using single-molecule localization microscopy (SMLM) on fixed, *in vitro* differentiated hepatocytes. Strikingly, we observed a *quasi*-periodic pattern of F-actin structures apparently crossing the lumen between two cells (Figure 1E). Because the SMLM has a z-resolution of ~500 nm and these structures are >1 µm in height, we can conclude that the F-actin projects into the BC lumen and does not correspond to rings around it, as in the Drosophila tracheal tube (Hannezo et al., 2015; Hayashi and Dong, 2017).

Ultra-structural analysis reveals a bulkhead-like pattern of transversal structures in the BC lumen physically connecting the apical surfaces of adjacent cells

Given the presence of both actin filaments and tight junctions (ZO-1) traversing the lumen, we investigated the structure of the apical surfaces of the juxtaposed cells in greater detail by electron microscopy (EM) on serial sections and 3D reconstructions of the entire lumen volume. Remarkably, the EM section of Figure 2A shows a branched lumen between three hepatocytes, with the characteristic glycogen granules, whose surfaces are connected by finger-like membrane processes. The fingers of one cell touch, or invaginate into, the opposing cell (Figure 2B) and the contact surfaces are sealed by tight junctions (Figure 2C, D). Interestingly, we observed that vesicles often accumulated at the base of these processes.

From a single section it is impossible to establish whether the lumen is continuous or divided into separate chambers. The 3D reconstruction (Figure 2E, Video Figure 2F, Suppl. Video S1) revealed that the transversal finger-like processes (Figure 2A) were sections of structures resembling the bulkheads of a boat. The bulkheads consisted of two parts, each contributed by the apical surface of one of the two adjacent cells which formed a ridge-shaped process (see 3D model Figure 2F, Video Figure 2F, Suppl. Video S1). Importantly, the two ridges were sealed by tight junctions which followed an unusual T-shape, with the horizontal bar representing the junctions longitudinal along the tube and the vertical bar the junctions extending along the

bioRxiv preprint doi: https://doi.org/10.1101/2020.12.31.424978; this version posted January 1, 2021. The copyright holder for this preprint (which was not certified by peer review) is the author/funder, who has granted bioRxiv a license to display the preprint in perpetuity. It is made available under aCC-BY-NC-ND 4.0 International license.

ridgeline (see scheme in Figure 2E, Video Figure 2F, Suppl. Video S1). The EM data are consistent with the presence of ZO-1 structures in the stripes crossing the lumen (Figure 1B). In some cases, the opposing processes are not precisely aligned along the ridgeline but shifted, forming a wide tight junction contact belt (Figure 2B, 2E, bulkheads B1, 4). The bulkheads can come either from the bottom (Figure 2F, bulkhead B3) or the top of the tube (Figure 2B, 2E, bulkheads B1, 2, 4), but never intersect it completely, thus ensuring lumen continuity in the BC (Video Figure 2F, Suppl. Video S1). Consequently, from the 3D reconstruction of Figure 2B and Suppl. Video S1, one can appreciate that the lumen has a tortuous shape. This accounts for the impression that the F-actin fluorescent and bright-field stripes only partially cross the lumen (Figure 1D). The *quasi*-periodicity of the bulkheads can therefore explain the actin pattern observed by live-cell imaging (Figure 1D) and SMLM (Figure 1E).

Altogether, the EM analysis revealed that adjacent hepatocytes are physically connected not only along the tight junction belt but also within the lumen via repetitive transversal connections between the apical surfaces sealed by tight junctions. These apical structures can therefore account for the high density of F-actin visualized by light microscopy (Figure 1C-E).

Transversal apical membrane structures form during BC lumen morphogenesis in embryonic liver

The repetitive pattern of bulkhead-like transversal connections could be a peculiar feature of the *in vitro* culture system, where the cells adhere to the same surface and are forced to form 2D layers. To verify that such organization has physiological relevance, we examined the ultrastructure of the nascent BC in the embryonic liver. Also here, EM on serial sections (Figure 3A, B) and 3D reconstruction of BC lumen (Figure 3C, D) in embryonic (E15.5) liver confirmed the existence of a bulkhead-like pattern of transversal connections. The lumen shape was even more complex than the one observed *in vitro*, due to the 3D organization of the tissue, with a higher degree of freedom for cell-cell contacts. Importantly, also *in vivo* the bulkheads did not divide the BC lumen into isolated chambers (Figure 3C, D). These results validate the structural organization of the hepatocytes observed *in vitro* and support the

bioRxiv preprint doi: https://doi.org/10.1101/2020.12.31.424978; this version posted January 1, 2021. The copyright holder for this preprint (which was not certified by peer review) is the author/funder, who has granted bioRxiv a license to display the preprint in perpetuity. It is made available under aCC-BY-NC-ND 4.0 International license.

conclusion that the two opposing apical surfaces are physically linked by transversal connections.

Conversion of hepatocyte polarity into simple apico-basal polarity

The formation of bulkhead-like apical processes *in vitro* and *in vivo* could be a specific feature of the tubular lumen of hepatocytes, as they were never described in simple epithelia, including cysts *in vitro*. In the developing liver, hepatoblasts can give rise either to hepatocytes generating BC or bile duct cells forming a tubular epithelium. When cultured *in vitro*, bile duct cells form 3D cysts with a spherical lumen (Huch et al., 2013; Prior et al., 2019; Tanimizu et al., 2007). Our aim was to exploit primary hepatoblasts to convert one type of cell polarity into another. To this end, we established an *in vitro* system that can recapitulate both hepatocyte and simple apico-basal polarity simultaneously, side by side in the same culture. To neutralize the effect of the ECM (Tanimizu et al., 2004, 2007) and focus on intrinsic cellular factors regulating the lumen shape, we used primary hepatoblasts under the same culture conditions. By optimizing the culture conditions (see Methods), the hepatoblasts that differentiated into hepatocytes formed branched BC-like structures at the bottom of the well (Figure 4A), whereas the bile duct (Sox9-positive) cells formed 3D cysts that rose from the bottom into the medium (Figure 4A', A'').

Having achieved an *in vitro* system that recapitulates the two types of cell polarity and lumen morphology, we set to identify genes required for these processes using an RNAi approach. To date, only a few genes have been associated with the regulation of hepatocyte lumen morphology (*Mark2/Par1b, Pard3, Stk11/Lkb1, Cdc42*) in hepatocyte cell lines, or primary hepatocytes (Cohen et al., 2004b; Fu et al., 2010; Wang et al., 2014; Yuan et al., 2009). We performed a focused screen on 25 candidate genes, including the aforementioned ones, encoding key regulatory components of cell polarity (Table S1): apical junction formation (e.g. Pard3, Tjp1, Cldn2), cytoskeleton regulation (e.g. Mark2/Par1b, Stk11/Lkb1, Cdc42) and polarized trafficking (e.g. Rab11a, Rab35, Cdc42). For the screen, we designed independent siRNA duplexes using customized software, selected six siRNAs with the highest functionality score per target gene and synthesized them with modifications to enhance their stability

bioRxiv preprint doi: https://doi.org/10.1101/2020.12.31.424978; this version posted January 1, 2021. The copyright holder for this preprint (which was not certified by peer review) is the author/funder, who has granted bioRxiv a license to display the preprint in perpetuity. It is made available under aCC-BY-NC-ND 4.0 International license.

(Farzan et al., 2017; Reynolds et al., 2004). Cells were transfected with the siRNAs and after 5 days in culture stained for F-actin, which is enriched at the apical domain (Figure 1C, D, 4A). Hit candidates were those yielding a penetrant lumen phenotype with a minimum of two siRNAs. Silencing of Ocln (Figure S4A) and Tjp1 (Figure S4B) yielded a loss of polarity, with de-localized F-actin and decreased intensity of the apical marker CD13 due to the absence of lumina. Remarkably, out of the 25 genes screened, silencing of Cdc42 and Rab35 did not compromise cell polarity, as judged by the localization of CD13 and ZO-1, but altered lumen morphology (Figure S4C, 4B, S4D). Cdc42 silencing caused dilated spherical lumina (Figure S4D, Table S1), thus reproducing the phenotype reported in liver-specific Cdc42 KO mice (Yuan et al., 2009), and validating our approach. However, Rab35 knock-down yielded the most striking phenotype, leading to the formation of large cyst-like structures (Figure 4B, S4D, and Video Figure 4B') instead of BC as in control (Luciferase, siLuc). Optical sectioning and 3D reconstruction showed that the lumen of these cysts was connected with the BC formed by the neighbouring hepatocytes (Figure 4C), indicating that the cells indeed displayed the two types of polarity side by side, reminiscent of the organization of the peri-portal zone of liver tissue (Antoniou et al., 2009; Müsch, 2018; Ober and Lemaigre, 2018). Rab35 is a versatile small GTPase, involved in numerous cellular processes related to cell polarity and lumen formation (Klinkert and Echard, 2016). Given the strength of the phenotype and because Rab35 had no previous connection to hepatocyte lumen morphology, we decided to focus on this gene and explore its function in more detail.

Rab35 is rate-limiting for the generation of hepatocyte lumina

To begin with, we validated the specificity of the Rab35 RNAi phenotype. First, out of six designed siRNAs, five yielded Rab35 mRNA down-regulation above 50% after 96h and showed various degrees of lumen alteration. The three siRNAs (siRab35 #2, #4, #5) that consistently yielded the strongest phenotype reduced Rab35 mRNA (Figure S4F) and protein level more than 70% (Figure 4D). Second, Rab35 was enriched in the apical surface of hepatocytes as well as lateral plasma membrane and cytoplasmic vesicles (Figure 4E), consistent with the reported endosomal localization (Klinkert et al., 2016; Kouranti et al., 2006). Upon silencing, this staining

bioRxiv preprint doi: https://doi.org/10.1101/2020.12.31.424978; this version posted January 1, 2021. The copyright holder for this preprint (which was not certified by peer review) is the author/funder, who has granted bioRxiv a license to display the preprint in perpetuity. It is made available under aCC-BY-NC-ND 4.0 International license.

was markedly reduced (Figure 4E). Third, expression of exogenous EGFP-tagged Rab35 yielded a similar pattern of localization (Figure 4F). Interestingly, Rab35 was not only enriched apically but also present on the transversal connections which were dynamically remodelled as the apical lumen expanded anisotropically (Figure 4F). Fourth, to further confirm that loss of Rab35 was specifically responsible for the observed phenotype, we performed a rescue experiment whereby we restored the expression of Rab35 by viral-mediated transduction of human Rab35, which is resistant to siRab35 #4. We quantified the effect of Rab35 knock-down on lumen morphology by measuring the radius of individual lumina in the control and knock-down conditions, and plotting the frequency distribution of values. There was a consistent shift towards larger lumina in the knock-down conditions by the three siRNA duplexes targeting Rab35 mRNA (Figure 4G). Importantly, in control conditions we could barely observe lumina with radius larger than 6 µm, whereas upon Rab35 silencing ~ 20–25% of lumina had a radius > than 6 µm. Adenovirus-mediated expression of EGFP-tagged Rab35 was able to rescue the Rab35 silencing phenotype, shifting the distribution of lumen radius towards the control, whereas expression of EGFP had no affect (Figure 4H). Altogether, these results suggest that Rab35 is rate-limiting for the generation of BC hepatocyte lumina and its depletion caused the formation of cyst-like structures similar to those formed by bile-duct cells *in vitro*.

Silencing of Rab35 causes the loss of transversal apical bulkheads and formation of spherical cysts via a cell self-organization process

To gain insights into the mechanism of Rab35 depletion on lumen morphogenesis, we imaged LifeAct-EGFP expressing cells transfected with Rab35 or Luciferase siRNA as control by live-cell time-lapse microscopy, as described above (Figure 1D, Figure S1). Whereas normal and control differentiating hepatoblasts transfected with Luciferase siRNA formed elongated lumina, upon Rab35 siRNA transfection, they generated spherical lumina, initially between two cells (Figure 5A, Video Figure 5A). With time, we could observe major cell rearrangements, whereby cells moved and reshaped their apical surface leading to the fusion of lumina and the formation of 3D multi-cellular cysts (Figure 5B, Video Figure 5B), as shown in Figure 4C. Also in this case, such a re-organization was not a result of cell division, as for other cysts formed *in*

bioRxiv preprint doi: https://doi.org/10.1101/2020.12.31.424978; this version posted January 1, 2021. The copyright holder for this preprint (which was not certified by peer review) is the author/funder, who has granted bioRxiv a license to display the preprint in perpetuity. It is made available under aCC-BY-NC-ND 4.0 International license.

vitro (Jewett and Prekeris, 2018), but rather by a self-organization process. A spherical expansion of the lumen occurred only in the cases where the cells failed to form the striped actin pattern indicative of the bulkheads typically present in BC lumina (Figure 5A, B, Video Figure 5A, 5B). Conversely, the elongated lumina that still formed always contained the transversal actin stripes. Careful inspection of the live cell imaging videos (e.g. Video Figure 1D, 5B) suggested that the disappearance of the transversal bulkheads precedes the formation of a spherical lumen.

To corroborate the loss of the bulkheads in the spherical lumina, we examined their ultra-structure by EM on serial sections and 3D reconstruction of the entire lumen volume. We focused on large cyst-like lumina formed by several cells. Individual EM sections of a cyst-like lumen between five cells showed that the bulkheads that are normally present in the BC lumina were absent (Figure 5C). This was confirmed by the 3D model of the lumen based on rendering plasma membranes and tight junctions (Figure 5D). In addition, the tight junctions between the cells did not protrude into the lumen, as seen at the sagittal cross section of the 3D model (Figure 5D).

These results suggest that down-regulation of Rab35 in differentiating hepatoblasts causes the loss of the transversal bulkheads and converts tubular BC lumina into cyst-like structures.

Down-regulation of Rab35 affects hepatocyte differentiation

The cyst-like structures generated upon Rab35 KD by differentiating hepatoblasts are reminiscent of the cysts formed by Sox9-positive primary bile duct cells *in vitro* (Figure 4A). This raises the question of whether loss of Rab35, in addition to modifying the cell polarity phenotype, also causes a change in the commitment of the hepatoblasts towards bile duct cells or, alternatively, a change in the hepatocyte cell fate. To address this question, we characterized the transcriptional profile of cells upon Rab35 silencing by RNA-seq analysis. We found 313 differentially transcribed genes in cells transfected with Rab35 siRNA compared to Luc siRNAs as control (Log_2 fold change cut-off 0.5, p-value cut-off 0.01). Strikingly, mature hepatocyte marker genes, e.g. *Serpina1, Ces1c, Pck1, Cyp3a11*, were down-regulated in

bioRxiv preprint doi: https://doi.org/10.1101/2020.12.31.424978; this version posted January 1, 2021. The copyright holder for this preprint (which was not certified by peer review) is the author/funder, who has granted bioRxiv a license to display the preprint in perpetuity. It is made available under aCC-BY-NC-ND 4.0 International license.

siRab35-transfected cells (Figure 6A, negative Log_2 fold change, magenta), whereas genes related to the apico-basal polarity in epithelial cells and typically not expressed in hepatocytes, were up-regulated (Figure 6A, positive Log_2 fold change, green), e.g. *Ap1m2, Mal, Grhl2* and *Rab25* (Fölsch et al., 1999; Ramnarayanan et al., 2007; Senga et al., 2012). Grhl2 was identified by Senga et al. (2012) as a bile duct cell-specific transcription factor, arguing that the cells acquire features of bile duct cells. This conclusion was confirmed by the finding that bile duct cells markers *Tacstd2* (*Trop2*) and *Krt19* (Segal et al., 2019) were also up-regulated. We verified the expression of various markers at the protein level by immunofluorescence specifically in the cells forming the cysts resulting from Rab35 silencing (Figure 6B). Some of the cells in the cysts continued to express Albumin (albeit at lower level), retained the accumulation of glycogen granules in the cytoplasm and did not have cilia (Figure 5C), suggesting that these hepatoblasts differentiated into hepatocytes and then changed cell fate towards bile duct cells. However, other cells were Krt19+/Alb- (outlined in Figure 6B), suggesting activation of the bile duct cells program in hepatoblasts. Yet, these cells did not express Sox9, an early marker of bile duct cells required for cilia formation (Antoniou et al., 2009; Poncy et al., 2015), indicating that they do not acquire a complete bile duct cell fate.

To understand to what extent Rab35 silencing alters the differentiation of hepatocyte progenitor cells, we compared the transcriptome of siRNA transfected cells (control and Rab35 siRNA, from Figure 6A) with that of three cell types, hepatoblasts, adult hepatocytes and bile duct cells. For this purpose, we performed gene set enrichment analysis (GSEA), a commonly used method for interpreting gene expression data (Mootha et al., 2003; Subramanian et al., 2005). GSEA calculates a so-called enrichment score, which reveals how strongly a given gene set is overrepresented among the highly-ranked genes in a list. When plotting the enrichment score, a rising curve at the left side of the graph indicates an overrepresentation at the top of the ranked gene list. In our analysis, all three ranked lists were generated using DESeq2 (Love et al., 2014) and reflect the gene expression profiles comparison between one cell type versus the other two. In the first step, we used GSEA to investigate the overrepresentation of the genes down-regulated upon Rab35 silencing in the three aforementioned cell types. The resulting enrichment plots (upper row of Figure 6C) clearly show the overrepresentation of the

bioRxiv preprint doi: https://doi.org/10.1101/2020.12.31.424978; this version posted January 1, 2021. The copyright holder for this preprint (which was not certified by peer review) is the author/funder, who has granted bioRxiv a license to display the preprint in perpetuity. It is made available under aCC-BY-NC-ND 4.0 International license.

investigated gene set in adult hepatocytes. In hepatoblasts, only a slight overrepresentation was detected, whereas in bile duct cells no enrichment was observable. Next, we repeated the analysis using the set of genes up-regulated upon Rab35 silencing. Interestingly, the resulting plots (the lower row of the Figure 6C) showed an overrepresentation of the investigated gene set in bile duct cells, while hardly any or no enrichment in the other two cell types could be detected. This confirms a positive correlation of gene expression profiles between transcriptomes of siRab35-transfected and bile duct cells.

In summary, the results show that silencing of Rab35 changed the transcriptional profile of the hepatoblasts, suggesting both a change from the default (*in vitro*) hepatocyte cell commitment towards the bile duct cell fate, but also a change in cell fate, through the transition from differentiated hepatocytes towards bile duct cells. Such a transition is not all-or-none, as in some cells it is more efficient than in others, and none acquires a complete bile duct cell fate.

Re-engineering of liver tissue architecture by silencing of Rab35 *in vivo*

The specific polarity of hepatocytes is a key element for the organization of liver tissue, particularly the formation of the BC network which is very distinct from other simple epithelia, including the bile duct. The change in cell polarity caused by the silencing of Rab35 in differentiating hepatoblasts *in vitro* provides a means to attempt to re-engineer liver tissue by modifying the BC lumen and cell self-organization *in vivo*. Therefore, we set to modify the polarity of hepatocytes by Rab35 silencing in the developing liver *in vivo*. The complete loss of Rab35 in a KO mouse line is embryonically lethal (Dickinson et al., 2016), presumably due to cytokinesis defects (Kouranti et al., 2006). To circumvent this problem and deplete Rab35 as *in vitro*, we took advantage of lipid nanoparticles (LNP) developed for human therapeutics, enabling the specific delivery of siRNAs to hepatocytes in the liver (Akinc et al., 2010; Zeigerer et al., 2012). To target the E13.5 embryonic liver, we used a method for *in utero* injection via vitelline vein (Ahn et al., 2018). We first validated the technique on mice expressing membrane-targeted GFP. We performed the *in utero* injection of LNP-GFP or Luciferase (as control) siRNA in E13.5 embryos and collected the livers after 4 days of development (Figure S7A). The GFP

bioRxiv preprint doi: https://doi.org/10.1101/2020.12.31.424978; this version posted January 1, 2021. The copyright holder for this preprint (which was not certified by peer review) is the author/funder, who has granted bioRxiv a license to display the preprint in perpetuity. It is made available under aCC-BY-NC-ND 4.0 International license.

signal in the liver was markedly and homogeneously reduced in hepatocytes, whereas different cell types, e.g. hematopoietic cells were unaffected (Figure S7B).

We next formulated the Rab35 siRNA validated *in vitro* (Figure 4D, G, H) and Luciferase siRNA into LNP and injected them into embryonic livers as described above. We analysed the effect on liver tissue using a pipeline of immunostaining, deep tissue imaging and 3D reconstruction (Morales-Navarrete et al., 2015) (Figure 7A). As in control liver, E17.5 livers injected with LNP-Luciferase siRNA developed normal elongated BC tubules formed by two adjacent hepatocytes (Figure 7A'). Strikingly, LNP-Rab35 siRNA-injection induced the formation of large tubular structures in the liver parenchyma (Figure 7A''). As these structures are remarkably similar to bile duct at this developmental stage, we needed to rule out that they may be formed by bile duct cells. First, the tubular structures are present throughout the parenchyma and distant from the portal area where the bile ducts are located. Second, staining with HNF4a and Sox9 confirmed that the cells forming the tubules expressed hepatocyte markers and were not fully differentiated bile duct cells (Figure 7A''' Suppl. Figure S7C), similar to the cells *in vitro* (Figure 5C, 6B). Importantly, the organization of the tubules suggested a change in cell polarity. Whereas in control tissue individual hepatocytes formed multiple lumina per cell (characteristic of hepatocyte polarity), the cells forming the large tubular structures polarized with a single apico-basal axis and shared the same apical lumen (Figure 7B, see below).

To demonstrate that the large tubular structures are not isolated but part of an interconnected luminal network, we performed 3D reconstruction of apical surfaces (marked with CD13) in 100 µm-thick sections (Figure 7B). In normal and LNP-Luciferase siRNA injected livers, CD13 had the typical appearance of 3D BC network (Figure 7C, Video Figure 7CD). In contrast, in Rab35 siRNA- injected livers, the 3D reconstruction revealed profound changes in lumen morphology in proximity to the central vein, i.e. distant from peri-portal bile duct (Figure 7D, Video Figure 7CD). The quantification from the reconstructed lumina showed a general increase in lumen radius (Figure 7E), similar to the one observed *in vitro* (Figure 4G). Remarkably, 30 ± 11 % of lumina had lumen radii significantly larger than the BC in the control

bioRxiv preprint doi: https://doi.org/10.1101/2020.12.31.424978; this version posted January 1, 2021. The copyright holder for this preprint (which was not certified by peer review) is the author/funder, who has granted bioRxiv a license to display the preprint in perpetuity. It is made available under aCC-BY-NC-ND 4.0 International license.

livers. 3D reconstruction of segments of large tubular structures confirmed that the tubes were formed by multiple cells, with an average of 4 cells sharing the same lumen (Figure 7F, G; Video Figure 7F). These results suggest that we succeeded in re-engineering liver tissue structure by down-regulation of Rab35 *in vivo.* This resulted in the modification of the cell polarity of hepatocytes which, instead of forming BC, self-organized into tubular epithelial structures similar to bile ducts.

Discussion

The mechanisms underlying the specific polarity of hepatocytes and the formation of BC are poorly understood, and different models including asymmetric cell division have been put forward (Fu et al., 2011; Li et al., 2016; Müsch, 2018; Ober and Lemaigre, 2018; Tanimizu and Mitaka, 2017). In the embryonic liver however, an almost fully connected BC network is generated despite hepatoblasts gradually ceasing to proliferate (Tanimizu et al., 2016; Yang et al., 2017, Figure 7C). Moreover, primary mature hepatocytes in culture can form a tubular BC network without significant cell division (Fu et al., 2010). In this study, we looked for a mechanism that could explain the peculiar tubular shape of hepatocyte apical lumina. We discovered the existence of very specific extensions of the apical membrane sealed by tight junctions in the lumen between two adjacent hepatocytes that fulfil the criteria for enabling the anisotropic elongation of the nascent BC tubule. The best analogy we could find for these structures are the bulkheads of of boats, ships and planes. Bulkheads provide structural stability and rigidity, strengthening the structure of elongated vessels. Here, the apical bulk-heads are *quasi*-periodic and can provide mechanical coupling between the apical surfaces of hepatocytes, which remain “clumped” together as the lumen grows. In their absence (upon Rab35 down-regulation), the apical surfaces of hepatocytes lose their anisotropic growth and the lumina convert from elongated into spherical, typical of simple epithelial cells. Our data thus suggest that mechanical coupling between hepatocytes underlies the formation of BC and provide unprecedented insights into the longstanding problem of epithelial morphogenesis of liver parenchyma.

bioRxiv preprint doi: https://doi.org/10.1101/2020.12.31.424978; this version posted January 1, 2021. The copyright holder for this preprint (which was not certified by peer review) is the author/funder, who has granted bioRxiv a license to display the preprint in perpetuity. It is made available under aCC-BY-NC-ND 4.0 International license.

In our culture setup, primary hepatoblasts differentiate into hepatocytes and recapitulate BC formation without cell division, as evidenced by live-cell imaging experiments. Hepatocytes initially form lumina between cell doublets. The lumina are closed and have no outlet to drain the inner fluid. Therefore, the increase in osmotic pressure resulting from the osmolytes pumped through the apical membrane should lead to a spherical lumen, not a tubular one. From the physics of thin-shells, formation of a tubular lumen with inner pressure and no outlets requires anisotropy of surface tension and/or rigidity of the wall (Berthoumieux et al., 2014; Landau and Lifshitz, 1986). The bulkheads are structural elements which can provide such anisotropy and mechanical stability to the elongating lumen under inner pressure. The position of the bulkheads could be determined by mechano-sensing mechanisms coupled to the tension and local curvature through the actin cortical mesh (Meyer et al., 2020). The bulkheads were detected in the embryonic liver, suggesting that they are not a cell culture artefact but have physiological relevance. The elongation of the apical lumen entails also the movement and re-arrangement of cell-cell contacts which is accompanied by the formation of new bulkheads (Figure 1D, S1C). Consistently, in the absence of bulkheads, lumina grow isotropically, generating cysts instead of rows of hepatocytes (Figure 5A and 5B).

The discovery of the apical bulkheads of hepatocytes focuses the attention on the mechanism underlying their formation. We obtained several cues from the morphological analysis and functional screen by RNAi. First, the bulkheads are characterized by a T-shaped arrangement of tight junctions which seal the two halves of the bulkheads (Figure 1B, 2F). To our knowledge, this organization is unprecedented in polarized cells. It is conceivable that the T-arrangement of the tight junctions could originate from the junctions longitudinal along the tubule (horizontal bar in the T) and zip-up along the ridgeline (vertical bar of the T), either from the bottom or from the top. Second, given that the tight junctions are connected to actin filaments, it is no surprise that the bulkheads contain F-actin transversally to the lumen elongation. The presence of F-actin in the bulkheads would introduce anisotropy in apical surface tension, leading to the formation of a tubular instead of spherical lumen. Live-cell imaging showed that the F-actin structures are dynamic and adaptable, and therefore, fit the requirements of a growing, branching and fusing BC network *in vivo*. The assembly of the

bioRxiv preprint doi: https://doi.org/10.1101/2020.12.31.424978; this version posted January 1, 2021. The copyright holder for this preprint (which was not certified by peer review) is the author/funder, who has granted bioRxiv a license to display the preprint in perpetuity. It is made available under aCC-BY-NC-ND 4.0 International license.

bulkheads would require that membrane is deposited to the apical surface which may be delivered by localized secretion or recycling from the endosomal system. Consistent with such a trafficking requirement, we observed the accumulation of vesicles at the base of the bulkheads. Third, by a focused RNAi screen for established regulators of cell polarity we found that the small GTPase Rab35, a regulator of endosomal recycling (Klinkert et al., 2016; Kouranti et al., 2006; Mrozowska and Fukuda, 2016), is required for the formation of the apical bulkheads and hepatocyte apical lumen shape.

In epithelial cells, Rab35 has been localized to the apical and lateral plasma membrane (Kouranti et al., 2006) and functionally associated with polarized trafficking and actin organization (Klinkert and Echard, 2016). In polarizing hepatoblasts, Rab35 is also enriched at the apical plasma membrane where the bulkheads are formed. However, whereas down-regulation of Rab35 in MDCK cysts led to an inversion of polarity (Klinkert et al., 2016), it did not cause a loss or inversion of polarity in hepatoblasts, but led to the disappearance of the bulkheads and the conversion from hepatocyte polarity to simple apico-basal polarity. These results suggest that Rab35 is rate-limiting for the formation of bulkheads in hepatocytes. Based on the previous work on Rab35 function (Klinkert and Echard, 2016; Kouranti et al., 2006), we envision that it could regulate the intracellular distribution and function of apical recycling endosomes to deliver transmembrane proteins, e.g. junction components, at the site of bulkheads initiation and/or growth. The presence of clusters of vesicles at the base of the bulkheads as visualized by EM supports this view. However, Rab35 is also known to coordinate membrane trafficking with the organization of the actin cytoskeleton (Chua et al., 2010; Klinkert and Echard, 2016). Therefore, Rab35 could regulate the nucleation and/or dynamics of the F-actin at the bulkheads. Testing these models will require a number of approaches, including taking advantage of previous studies on genes regulating hepatocyte polarity. Lkb1 was shown to be part of a molecular pathway including cAMP-Epac-MEK-AMPK regulating BC network formation (Fu et al., 2010, 2011; Homolya et al., 2014; Woods et al., 2011). Pard3, Par1b and various Claudins were reported to have an effect on the hepatocyte polarity, when depleted in different hepatocyte cell lines (Can10, HepG2, and WIFB9) and primary adult hepatocytes (Grosse et al., 2013; Slim et al., 2013; Son et al., 2009; Wang et al., 2014). The function of these

bioRxiv preprint doi: https://doi.org/10.1101/2020.12.31.424978; this version posted January 1, 2021. The copyright holder for this preprint (which was not certified by peer review) is the author/funder, who has granted bioRxiv a license to display the preprint in perpetuity. It is made available under aCC-BY-NC-ND 4.0 International license.

genes should thus be re-visited in the context of the bulkheads and anisotropy of lumen elongation. It will be important to explore the role of the actin cytoskeleton, for example via a variety of drugs, under condition that they do not disrupt polarity or generate pleiotropic cytotoxic effects. The role of Rab35 may be mediated by its known effectors regulating the actin cytoskeleton (e.g. MICAL1 and OCRL; Chaineau et al., 2013; Dambournet et al., 2011; Frémont et al., 2017) or unknown hepatocyte-specific effectors. In this respect, the transcriptomics analysis revealed a wide number of candidate genes differentially expressed in hepatocytes vs. bile duct cells, and up- or down-regulated upon Rab35 silencing. Dissecting the mechanisms of bulkheads formation will thus necessitate a molecularly-broad experimental strategy.

Remarkably, silencing of Rab35 not only changed the lumen morphology of polarizing hepatoblasts *in vitro*, but also allowed us to re-engineer the organization of the developing liver parenchyma which displayed a striking increase of large tubular structures resembling bile ducts. This means that we succeeded in converting the polarity of hepatocytes into simple apico-basal polarity also *in vivo*. Surprisingly, Rab35 depletion also altered the commitment of hepatoblasts towards bile duct cells and/or switched hepatocytes towards the bile duct cell program, although incompletely. Some cells retained hepatocyte features, whereas others did express bile duct cell markers, but not Sox9 required for cilia formation. We cannot determine whether Rab35 down-regulation directly poises the hepatoblasts towards the bile duct cell fate or this is a consequence of the change in cell polarity. One possibility is that the lumen morphology is sensed by the polarizing hepatoblasts, e.g. via a mechanosensing pathway that feedbacks on the cell transcriptional program. Interestingly, in retinal neuroepithelia and pancreas, cell fate decision could be manipulated by changing the size of the apical domain, that was reflected on the activity of the Notch signalling pathway (Clark et al., 2012; Löf-Öhlin et al., 2017). Besides Rab35, other well established cell polarity proteins, Crb3 and Cdc42, can directly or indirectly influence the cell fate of progenitor cells (Szymaniak et al., 2015, Kesavan et al., 2009). While Crb3 regulates the cell fate of airway epithelial cells by directly interacting with components of the Hippo pathway (Szymaniak et al., 2015), Cdc42 plays a cell non-

bioRxiv preprint doi: https://doi.org/10.1101/2020.12.31.424978; this version posted January 1, 2021. The copyright holder for this preprint (which was not certified by peer review) is the author/funder, who has granted bioRxiv a license to display the preprint in perpetuity. It is made available under aCC-BY-NC-ND 4.0 International license.

autonomous role in the specification of pancreatic progenitors by controlling their surrounding microenvironment.

Our data provide yet another example for the complex interplay between cell polarity, cell fate decision and mechanics in tissue self-organization, and provide new insights into liver tissue organization both in development and in the adult. The apical bulkheads appear to be a distinctive feature of the hepatocytes and the BC network. The dynamics of the apical bulkheads and the role of actin filaments and associated factors will be crucial to elucidate the interplay between cellular morphogenesis and cell and tissue mechanics. Additionally, the bulkheads could serve as hot-spots of contractility to facilitate bile flux, as shown *in vivo* (Meyer et al., 2017; Watanabe et al., 1991). The bulkheads in ships can also act as (semi)watertight compartments to prevent seeping of water to other parts of the ship. Similarly in the BC, they could act as valves ensuring directionality of bile flux in a non-peristaltic contractility. Understanding their structure and function will thus provide novel information on the role of the acto-myosin system in the regulation of bile flux in the BC network.

Acknowledgements

We are grateful to Arnaud Echard for discussions and sharing various reagents. We thank Drs. Meritxell Huch, Elisabeth Knust, Kai Simons, Ivan Baines, and Janelle Lauer for stimulating discussions and critical reading of the manuscript. We acknowledge Sandra Segeletz for sharing her expertise in recombinant adenovirus production and live-cell imaging and Alexandra Kalaidzidou for visualization artwork. We acknowledge the DRESDEN-concept Genome Center for the bulk RNA-sequencing service and for the support of the Light Microscopy Facility, a Core Facility of the CMCB Technology Platform at TU Dresden. We would like to thank the following Services and Facilities of the Max Planck Institute of Molecular Cell Biology and Genetics for their support: Antibody Facility, Biomedical Services, Electron Microscopy Facility, Light Microscopy Facility, Protein Expression, Purification and Characterization (PEPC) Facility, and Scientific Computing Facility, particularly Lena Hersemann and Noreen Walker.

This research was financially supported by the German Federal Ministry of Research and Education (BMBF) (LiSyM, grant number 031L0038), the European Research Council (ERC) (grant number 695646), Deutsche Forschungsgemeinschaft (DFG, German Research

bioRxiv preprint doi: https://doi.org/10.1101/2020.12.31.424978; this version posted January 1, 2021. The copyright holder for this preprint (which was not certified by peer review) is the author/funder, who has granted bioRxiv a license to display the preprint in perpetuity. It is made available under aCC-BY-NC-ND 4.0 International license.

Foundation) under Germany´s Excellence Strategy – EXC-2068– 390729961– Cluster of Excellence Physicsof Life of TU Dresden and the Max Planck Society (MPG).

Author contributions

Conceptualization, M.Z., L.B. and Y.K.; Methodology, L.B., J.D. and S.S.; Investigation, L.B., U.R., J.D., S.S., J.I.V., C.F. and H.R.; Software, E.G., H.M-N. and J.I.V; Formal analysis, L.B., U.R., E.G., H.M-N., J.I.V, C.F. and Y.K.; Resources, T.Z., E.S., T.P., V.K. and M.V.; Visualization, L.B., U.R., E.G., M.V., J.I.V., H.M-N., C.F. and Y.K.; Validation, L.B.; Writing – Original draft, L.B.; Writing – Review and Editing, M.Z. and Y.K.; Funding acquisition, M.Z.

Declaration of interests

The authors declare no competing interests.

Figure titles and legends

Figure 1: Lumen morphogenesis in hepatocytes is accompanied by specific actin structures that interconnect the two lumen-forming cells (See also Figure S1)

A) Schematic overview of primary Dlk+ hepatoblasts in Matrigel sandwich culture differentiating into hepatocytes and recapitulating BC formation.
B) Differentiated hepatocytes form branched interconnected BC lumina. Immunofluorescence microscopy images of differentiated hepatocytes stained for F-actin with Phalloidin-Alexa488, and for apical markers CD13 and ZO-1. Scale bar: 10 µm.
C) *In vitro* differentiated hepatocytes express mature hepatocyte markers and down-regulate the hepatoblast marker Dlk. Heatmap comparing the expression of selected hepatocyte marker genes in primary Dlk+ hepatoblasts (Hepatoblasts), *in vitro* differentiated hepatocytes (Diff. hepatocytes) and control mature hepatocytes isolated from adult mouse livers (Mature hepatocytes). RNA-seq experiment in 4 biological replicates.
D) Images from live-cell time-lapse microscopy documenting the formation of BC between two differentiating hepatoblasts expressing LifeAct-EGFP. During imaging, the extending tubular lumen displayed a bulge at 27h from the start of imaging, which was subsequently ”re-absorbed”. The insert **D’** shows individual frames taken each 10 min from this timepoint, documenting the recovery of the tubule (white star). Note the transverse striped pattern in brightfield and actin channels, which is apparent when the lumen is tubular but not observed within the bulge. Scale bar: 10 µm. See also Video Figure 1D (Scale bar: 10 µm).

bioRxiv preprint doi: https://doi.org/10.1101/2020.12.31.424978; this version posted January 1, 2021. The copyright holder for this preprint (which was not certified by peer review) is the author/funder, who has granted bioRxiv a license to display the preprint in perpetuity. It is made available under aCC-BY-NC-ND 4.0 International license.

E) Single-molecule localization microscopy (SMLM) image of a lumen between two differentiated hepatocytes, actin labelled with Phalloidin-Alexa647. Note the transverse striped actin pattern. Scale bar: 5 µm.

Figure 2: Ultra-structural analysis reveals a bulkhead-like pattern of transversal structures sealed by T-shaped tight junctions in the BC lumen

A) Electron microscopy image of a BC branched between three cells. Longitudinal section of *in vitro* differentiated hepatocytes. GG: glycogen granules. The outlined region is shown in panel B. Scale bar: 5 µm.
B) Section of BC formed by two cells from a series of longitudinal 90-nm sections shown in Bi-Biv. The highlighted regions with transversal membrane connections are shown in the panel **C** and **D**. The membrane connections are not visible in every section **(Bi-Biv)**. Scale bar: 1 µm.
C) and **D)** Detailed view of the outlined regions in panel **B**. Membrane connections are formed by apical surfaces of both cells lining the BC and include the tight junctions (TJ, arrows). Vesicles (V) are often observed to accumulate in the vicinity of the connections. Scale bar: 1 µm.
E) 3D reconstruction of serial sections in **B (Bi-Biv)** based on apical plasma membranes and tight junctions rendering. The cytoplasm of the lumen-forming cells is in green and blue, the tight junctions are highlighted in red. See also Suppl. Video S1.
F) Simplified model of BC based on the 3D reconstruction in **E** with periodic bulkhead-like membrane connections formed from the top or the bottom of the lumen (arrowheads). The tight junctions (red) have a T-shape, with the junctions longitudinal along the tube connected with the junctions extending along the ridgeline within each bulkhead. Uninterrupted flow within the lumen between bulkheads is shown with a dotted line. See also Video Figure 2F.

Figure 3: Transversal apical membrane structures form during BC lumen morphogenesis in embryonic liver

A) and **B)** Electron microscopy images of two serial sections of a forming BC in a E15.5 liver, surrounded by tight junctions (white arrows). The lumen of the two adjacent hepatocytes is outlined in white. The black arrows point to the tight junctions within the bulkhead-like membrane connections B1 and B2. Scale bar: 500 nm.
C) and **D)** 3D model of the lumen in A. and B., based on lumen surface rendering on serial sections. At the left bottom side (dashed black line), the BC continues. White arrows indicate the bulkheads B1, B2 shown in A. and B., respectively. Scale bar: 500 nm.

Figure 4: Conversion of hepatocyte polarity into simple apico-basal polarity (See also Figure S4)

bioRxiv preprint doi: https://doi.org/10.1101/2020.12.31.424978; this version posted January 1, 2021. The copyright holder for this preprint (which was not certified by peer review) is the author/funder, who has granted bioRxiv a license to display the preprint in perpetuity. It is made available under aCC-BY-NC-ND 4.0 International license.

A) Validation of the culture system. A mixture of primary hepatoblasts and bile duct cells form BC and cysts under the same culture conditions. Images at different z-positions demonstrate that cysts grow in the z-direction (A', A''), while hepatocytes with BC form a cell-layer close to the well bottom. Cells stained for F-actin with Phalloidin-Alexa488. Scale bar: 10 µm. Schematics represent XZ view.
B) Knock-down of Rab35 in differentiating hepatoblasts caused formation of cyst-like structures (B'), whereas cells treated with the control siRNA (siLuc) were unaffected and formed BC. Microscopy images of cells stained for F-actin with Phalloidin-Alexa488. Scale bar: 30 µm. See also Video Figure 4B' (Scale bar: 30 µm).
C) 3D reconstruction of the cells treated with Rab35 siRNA show the variability of the phenotype from enlarged swollen lumina to spherical cyst-like structures growing in the z-direction (lumina stained with the apical marker CD13). The BC connected to the cyst, reminiscent of the organization of the peri-portal zone in liver tissue.
D) Three independent Rab35 siRNA duplexes down-regulate Rab35 protein levels by 73% ± 3% (n = 3, error bars: SD). Representative Western blot and quantification of protein knock-down.
E) Microscopy images of differentiated hepatocytes treated with Luciferase or Rab35 siRNA stained with Rab35 antibodies (yellow). Rab35 localizes to the apical and lateral plasma membrane and cytoplasmic puncta. The levels of Rab35 are markedly reduced in the cyst-like structures formed upon Rab35 siRNA transfection.
F) Localization of exogenous EGFP-Rab35 in polarizing hepatoblasts. Scale bar: 10 µm.
G) Histogram of the local lumen radius in control cells and cells treated with Rab35 siRNA estimated based on microscopy image analysis. Rab35 knock-down by three independent siRNAs results in the shift towards the lumina with larger radius (n= 3 (with 4 images per condition), error bars: SEM).
H) The enlarged lumina phenotype in the cells treated with Rab35 siRNA is rescued by expression of human Rab35-EGFP from recombinant adenovirus. Frequency curve of the lumen radius (yellow) overlaps with the one of the control cells expressing EGFP only. EGFP alone does not affect the lumen enlargement caused by Rab35 knock-down (red). (n= 3 (with 4 images per condition), error bars: SEM).

Figure 5: Silencing of Rab35 causes the loss of the transversal apical membrane bulkheads and formation of spherical cysts via a cell self-organization process

A) In the cells treated with Rab35 siRNA, the lumina tend to grow as spheres instead of elongating as tubes. Images from the live-cell time-lapse microscopy experiment showing two neighbouring differentiating hepatoblasts expressing LifeAct-EGFP under Rab35 siRNA conditions. The white star indicates the forming lumen between the two cells. Note that the

bioRxiv preprint doi: https://doi.org/10.1101/2020.12.31.424978; this version posted January 1, 2021. The copyright holder for this preprint (which was not certified by peer review) is the author/funder, who has granted bioRxiv a license to display the preprint in perpetuity. It is made available under aCC-BY-NC-ND 4.0 International license.

typical transverse striped actin pattern observed in the tubular BC is absent. Scale bar: 10 µm. See also Video Figure 5A (Scale bar: 10 µm).

B) Multicellular cyst-like structures form by cell re-arrangements. Images from the live-cell time-lapse microscopy experiment. The cells self-organize in such a way that the three separate lumina (black star) eventually fuse into one large spherical lumen, in the absence of cell division. Scale bar: 10 µm. See also Video Figure 5B (Scale bar: 10 µm).

C) EM analysis of a cyst-like lumen resulting from the Rab35 knock-down. Three serial longitudinal 90-nm sections of the lumen formed between five cells. The bulkheads typical for hepatocyte BC are absent in the lumen. Arrows indicate tight junctions. GG: glycogen granules. Scale bar: 5 µm.

D) A longitudinal view through the middle of a 3D model of the lumen based on rendering plasma membranes and tight junctions (red) on serial sections. The five cells forming the lumen are represented in different colours (cyan, violet, yellow, blue and green). Red arrows point to the tight junctions at which the cyst is cut open to reveal the sagittal view in (D).

E) A sagittal view of the lumen. The lumen has a circular profile and tight junctions do not protrude into the lumen.

Figure 6: Down-regulation of Rab35 affects hepatocyte differentiation

A) Volcano-plot showing up- and down-regulated genes upon Rab35 siRNA treatment compared to the control siRNA. The marker genes for hepatocytes are down-regulated (magenta, e.g. *Serpina1e, Ces1c, Pck1, Cyp3a11*), whereas genes typically not expressed in hepatocyte but in other epithelial cell types are up-regulated (green, e.g. A*p1m2, Grhl2, Rab25, Krt19*).

B) Immunofluorescence microscopy images of a cyst-like structure compared to the control cells. In the cyst, some cells are positive for Krt19 (white outline) and have almost no albumin expression. In the control, Krt19 is barely detected. Scale bar: 10 µm.

C) Enrichment plots from Gene set enrichment analysis (GSEA) to test whether differentially expressed genes in **A** are enriched in gene expression profiles of hepatocytes, hepatoblasts or bile duct cells. The down-regulated genes (magenta) are over-represented in hepatocytes, whereas the up-regulated genes (green) are enriched in the bile duct cell gene expression profile. P-values are included above the GSEA curve.

Figure 7: Silencing of Rab35 *in vivo* results in altered cell polarity and liver tissue architecture (See also Figure S7)

A) Immunofluorescence images of liver tissue collected 4 days after *in utero* injection of Luciferase (siLuc) and Rab35 (siRab35) siRNAs formulated into LNP via vitelline vein in E13.5

bioRxiv preprint doi: https://doi.org/10.1101/2020.12.31.424978; this version posted January 1, 2021. The copyright holder for this preprint (which was not certified by peer review) is the author/funder, who has granted bioRxiv a license to display the preprint in perpetuity. It is made available under aCC-BY-NC-ND 4.0 International license.

embryos. The square on the low magnification images (scale bar: 500 µm) shows where the high resolution image was taken (scale bar: 20 µm). Imaged areas are located in the liver parenchyma, devoid of bile duct cell marker Sox9. The inserts (scale bar: 20 µm) in panels **A'** and **A''** show the difference between BC and bile duct-like lumina in LNP-siRab35 injected liver. Panel **A'''** compares tubular lumina in the parenchyma to the bile duct lumina in the portal area (Sox9-positive).

B) Immunofluorescence images of liver tissues from **A** show examples of hepatocyte polarity in the control tissue (a single hepatocyte forms multiple lumina per cell) and simple apico-basal polarity in LNP-siRab35 injected liver (cell have a single apical domain oriented towards a shared lumen).

C) and **D)** 3D reconstruction of lumina labelled with an apical marker CD13 in 100 µm-thick sections of liver tissue injected with LNP-siLuc (**C**) and LNP-siRab35 (**D**). Scale bar: 30 µm. See also Video Figure 7CD.

E) Quantification of the lumen radius distribution based on the 3D reconstructions such as in C and D (n= 3, error bars: SEM).

F) 3D reconstruction of a tubule found in LNP-siRab35 injected livers shows lumen in green surrounded by multiple cells. See also Video Figure 7F.

G) Quantification of number of cells surrounding the lumen in relation to lumen radius and position along the tubule.

Supplemental figure titles and legends

Figure S1 (Related to Figure 1): Live-cell video microscopy images of BC morphogenesis in LifeAct-EGFP expressing cells

A) A single polarizing differentiating hepatoblast forming multiple tubular lumina. Scale bar: 10 µm. See also Video Figure S1A.

B) BC network grows between neighbouring cells by fusion and branching (marked by star) of elongated tubular lumina. Scale bar: 10 µm. See also Video Figure S1B.

C) A lumen formed between two cells starts growing spherical, but is later adjusted and continue to elongate as a typical BC lumen. Scale bar: 10 µm. See also Video Figure S1C.

Figure S4 (Related to Figure 4): Conversion of hepatocyte polarity into simple apico-basal polarity

A) Down-regulation of Occludin impairs the lumen formation in differentiating and polarizing hepatobalsts. Immunofluorescence images of cells stained for the apical marker CD13 and Occludin. Scale bar: 10 µm.

bioRxiv preprint doi: https://doi.org/10.1101/2020.12.31.424978; this version posted January 1, 2021. The copyright holder for this preprint (which was not certified by peer review) is the author/funder, who has granted bioRxiv a license to display the preprint in perpetuity. It is made available under aCC-BY-NC-ND 4.0 International license.

B) Down-regulation of the tight junction protein ZO-1 impairs the lumen formation in differentiating and polarizing hepatobalsts. Immunofluorescence images of cells stained for ZO-1. Scale bar: 10 µm.
C) Down-regulation of Cdc42 leads to spherical lumina instead of BC in polarizing hepatoblasts. The polarity is not perturbed, as apical markers CD13 and ZO-1 still localized to the formed lumina. Scale bar: 10 µm.
D) Down-regulation of Rab35 leads to profound changes in lumen morphology of polarizing and differentiating hepatoblasts. The cells form multicellular structures with a shared lumen positive for apical markers CD13 and ZO-1. Immunofluorescence images of cells treated with three different siRNAs oligos. Scale bar: 10 µm.
E) Estimation of knock-down efficiency of six siRNAs designed to target Rab35 mRNA 96h post-transfection in differentiating and polarizing hepatoblasts *in vitro* (n =2, SD).

Figure S7 (Related to Figure 7): *In utero* injection method validated by silencing of GFP in GFP-expressing mouse line

A) Schematic overview of *in utero* injection experiments.
B) Microscopy images showing the down-regulation of GFP in GFP expressing mouse livers via *in utero* injection of LNP-siGFP in comparison to livers injected with control LNP-siLuc. Scale bar: 30 µm.
C) Immunofluorescence microscopy images of the livers injected with LNP-siRab35 and stained for HNF4a (yellow) and Sox9 (magenta). Scale bar: 30 µm.

Star Methods

Lead Contact

Further information and requests for resources and reagents should be directed to and will be fulfilled by the Lead Contact, Marino Zerial (zerial@mpi-cbg.de).

Materials Availability

All unique/stable reagents generated in this study are available from the Lead Contact with a completed Materials Transfer Agreement.

Data and Code Availability

Bulk RNA-sequencing data will be deposited to the NCBI Gene Expression Omnibus (GEO) under accession number GEO upon acceptance. Code for the scripts will be made available upon acceptance.

bioRxiv preprint doi: https://doi.org/10.1101/2020.12.31.424978; this version posted January 1, 2021. The copyright holder for this preprint (which was not certified by peer review) is the author/funder, who has granted bioRxiv a license to display the preprint in perpetuity. It is made available under aCC-BY-NC-ND 4.0 International license.

Experimental Model and Subject Details

Animals and animal handling

Animal experiments were conducted in accordance with German animal welfare legislation in pathogen-free conditions in the animal facility of the MPI-CBG, Dresden, Germany. Mice were maintained in a conventional barrier animal facility with a climate-controlled environment on a 12-h light/12-h dark cycle, fed ad libitum with regular rodent chow. Protocols were approved by the Institutional Animal Welfare Officer (Tierschutzbeauftragter), and necessary licenses were obtained from the regional Ethical Commission for Animal Experimentation of Dresden, Germany (Tierversuchskommission, Landesdirektion Dresden).

For primary hepatoblast isolations, embryonic livers were collected from time-pregnant (E13.5-E14.5) wild-type mice C57BL/6JOlaHsd (Harlan laboratories/Envigo, USA) or C57BL6/JRj (Janvier Labs, France), or transgenic lines LifeAct-EGFP (Riedl et al., 2010), ROSAmT/mG (Muzumdar et al., 2007) or the incross of the two transgenic lines. For *in utero* LNP injection experiments, the GFP-expressing embryos were generated by crossing of ROSAmT/mG female with PGKCre(J) male (Lallemand et al., 1998). The transgenic or wild-type embryos were injected *in utero* via vitelline vein at E13.5 and livers collected at E16.5 – E17.5.

Primary hepatocytes

Primary hepatocytes were isolated from male 8-12 week-old mice according to the established protocol (Klingmüller et al., 2006) and processed immediately for RNA isolation.

Chol/L cell line

Large cholangiocyte (bile duct cell) cell line (Ueno et al., 2003) was cultured as monolayer or in a 100% Matrigel drop in DMEM + GlutaMAX High Glucose (Cat. No. 31966, Gibco), 5% FBS (heat inactivated), 10 mM HEPES, 1x NEAA (Cat. No. 11140-050, Gibco).

QBI-239A

Cell line was cultured in DMEM High Glucose (Cat. No. 41966-029, Gibco) with 5% FBS (heat inactivated) and used for the production of adenovirus.

bioRxiv preprint doi: https://doi.org/10.1101/2020.12.31.424978; this version posted January 1, 2021. The copyright holder for this preprint (which was not certified by peer review) is the author/funder, who has granted bioRxiv a license to display the preprint in perpetuity. It is made available under aCC-BY-NC-ND 4.0 International license.

Method Details

Dlk+ hepatoblast isolation

Hepatoblasts were isolated as Dlk+ fraction using magnetic cell separation. The protocol was adapted from Tanimizu et al. (2003) with several changes. Timed-pregnant mice (E13.5-14.5) were sacrificed by cervical dislocation. 16-24 embryonic livers were collected, fragmented and incubated in Liver perfusion media (Thermo Fisher Scientific, Cat. No. 17701-038) for 20 min in a 37°C water bath. The liver pieces were digested in Liver Digest Medium (Thermo Fisher Scientific, Cat. No. 17703-034,) supplemented with 10 µg/ml DNAse I (cat. No. DN25, Sigma-Aldrich) for further 20 min. Erythrocytes were lysed in Red blood cell lysis buffer (155 mM NH_4Cl, 10 mM $KHCO_3$, 0.1 mM Na_4EDTA, pH 7.4). Digested cells were incubated with blocking antibody Rat Anti-Mouse CD16/CD32 (BD Biosciences, Cat. No. 553142, 1:100) for 10 min, then with Anti-Dlk mAb-FITC (MBL, Cat. No. D187-4, 1:40) for further 15 min. After washing with a buffer (0.5% BSA, 2 mM EDTA in PBS), cells were incubated with Anti-FITC MicroBeads (Miltenyi Biotec, Cat. No. 130-048-701, 1:10) for 15 min and separated on a magnetic column (Miltenyi Biotec, Cat. No. 130-024-201) according to the manufacturer's protocol.

Hepatoblasts culture and differentiation

Culture wells were pre-coated with Matrigel (BD Biosciences, Cat. No. 356231, 10% Matrigel in PBS) for 30 min at 37°C and washed with PBS. Dlk+ enriched cells were seeded in Expansion media (DMEM/F-12, GlutaMAX™ supplement (ThermoFisher, Cat. No. 31331028), 10% FBS, 1x ITS-X (Gibco, Cat. No. 51500-056), 0.1 µM Dexamethasone (Sigma-Aldrich, Cat. No D1756-25MG,), 10 mM Nicotinamide (Sigma-Aldrich, Cat. No. N0636-100G), 10 ng/ml human HGF (in-house production), 10 ng/ml mouse EGF (in-house production). In 96-well plates, cells were seeded at the density 13 000 cells/well, in 24-well plates at the density 60 000 cells/well. 24h later, the cells were overlaid with Differentiation media (MCDB131, no glutamine, (Gibco, Cat. No. 10372019), 5% FBS, 2 mM L-glutamine (ThermoFisher, Cat. No. M11-004), 1x ITS-X (Gibco, Cat. No. 51500-056), 0.1 µM Dexamethasone (Sigma-Aldrich, Cat. No D1756-25MG)) containing

bioRxiv preprint doi: https://doi.org/10.1101/2020.12.31.424978; this version posted January 1, 2021. The copyright holder for this preprint (which was not certified by peer review) is the author/funder, who has granted bioRxiv a license to display the preprint in perpetuity. It is made available under aCC-BY-NC-ND 4.0 International license.

Matrigel to the final 5%. Cells were cultured for 5 days at 37°C, 5% CO_2 with one additional Differentiation media change. Dlk+ cells from E14.5 livers contained ~ 10% cells positive for bile duct cell marker Sox9 and were used in the experiments to optimize the growth of bile duct cysts. For other experiments, Dlk+ cells from E13.5 livers were used, as all the cells gave rise to hepatocytes with BC in the above culture conditions.

Live-cell time-lapse microscopy

For the live-cell video microscopy, LifeAct-EGFP (Riedl et al., 2010) and ROSAmT/mG (Muzumdar et al., 2007) mouse strains were crossed and EGFP+ embryos were collected for the Dlk+ cells' isolation. The Dlk+ cells were plated (transfected with siRNA) and imaged from the day 3 of the culture at an epifluorescent microscope Zeiss Axiovert 200 M with an incubator (37°C, 5% CO_2) using an 20x objective (NA 0.5) in 10 min intervals for approximately 52 h. To image the localization of EGFP-Rab35, the Dlk+ cells were isolated from ROSAmT/mG embryos and transduced with a recombinant adenovirus (AdenoEGFP-Rab35) at day 2 of the culture. The cells were imaged on the day 3 in 5 min intervals for up to 24h.

Immunofluorescence staining and confocal imaging

Cultured cells were fixed with 3% PFA for 15 min at RT, washed 3x with PBS, permeabilized with 0.1% Triton X-100 in PBS for 5 min at RT, and blocked with 0.5% FBS in PBS for min 30 min at RT. Primary antibodies were diluted in the blocking solution, rat monoclonal anti-CD13 (Novus, Cat. No. NB100-64843, 1:500), rabbit polyclonal anti-ZO-1 (Thermo Fisher Scientific, Cat. NO. 40-2200, 1:200), rat monoclonal anti-Cytokeratin 19 (Sigma-Aldrich, Cat. No. MABT913, 1:500) and goat polyclonal anti-Albumin (Novus, Cat. No. NB600-41532, 1:200) and were incubated 1h at RT or overnight at 4°C. Secondary antibodies (and/or Phalloidin-Alexa dyes (Thermo Fisher Scientific, 1:250) and DAPI (1 mg/ml, 1:1000)) were incubated for 1h at RT. For staining with rabbit polyclonal anti-Rab35 (Antibody Facility MPI-CBG Dresden, H26952, 1: 1000), the cells were permeabilized with 0.05% saponin and blocked with 3% BSA in PBS instead. Finally, cells were washed with PBS and imaged on laser scanning confocal microscopes Olympus Fluoview

bioRxiv preprint doi: https://doi.org/10.1101/2020.12.31.424978; this version posted January 1, 2021. The copyright holder for this preprint (which was not certified by peer review) is the author/funder, who has granted bioRxiv a license to display the preprint in perpetuity. It is made available under aCC-BY-NC-ND 4.0 International license.

1000 (objectives 40x/0.9/air, 60x/1.2/water), Zeiss LSM 700 (objectives 40x/1.2/water, 20x/0.8/air).

Single-molecule localization microscopy

Single-molecule localization microscopy (SMLM) experiments were performed on a Nikon Eclipse Ti microscope, which is specified elsewhere in detail (Franke et al., 2019). Prior to acquisition, samples were irradiated in epifluorescence illumination mode to turn emitters, which were out-of-focus in the acquisition HILO illumination scheme, into the dark state. The length of the acquisition was set to capture the majority of emitters, i.e. imaging was concluded when only a very minor number of active emitters was detectable. When a critically low spot density was first reached, an acquisition scheme of 1 frame with low 405 nm excitation (activation) followed by 5 consecutive frames with 641 nm excitation, was used. Typical acquisition lengths were 60000-200000 frames with 20 ms integration time and 641 nm excitation. Raw image stacks were analysed with rapidSTORM 3.2 (Wolter et al., 2012). The FWHM was set as a free fit parameter, but in the limits of 275–650 nm, which corresponds to an axial range of approximately 1µm (Franke et al., 2016), the fit window radius was set to 1200 nm, the intensity threshold to 1000 photons, while all other fit parameters were kept from the default settings in rapidSTORM 3.2. Linear lateral drift correction was applied by spatio-temporally aligning distinct structures to themselves. This was facilitated by color-coding of the temporal coordinate with the built-in tool.

Transmission electron microscopy

In vitro cultures of hepatoblasts grown in 24-well plates were fixed by adding warm 2% glutaraldehyde in 200 mM HEPES, pH 7.4 to the culture medium at a 1:1 ratio and incubated for 5 min at 37 °C. Then the fixative and medium mixture was replaced by adding fresh 1% glutaraldehyde in 200 mM HEPES, pH 7.4 and samples incubated at 37 °C for another 2 hours, then at room temperature overnight. For resin embedding samples were post-fixed with 1% osmium tetroxide and 1.5% potassium ferricyanide for 1 hour on ice, then contrasted en-bloc with 2% aqueous uranyl acetate for 2 hours at room temperature, dehydrated with a graded

bioRxiv preprint doi: https://doi.org/10.1101/2020.12.31.424978; this version posted January 1, 2021. The copyright holder for this preprint (which was not certified by peer review) is the author/funder, who has granted bioRxiv a license to display the preprint in perpetuity. It is made available under aCC-BY-NC-ND 4.0 International license.

ethanol series: 70-80-90-96%, each for 10 min, and 4x 100%, each for 15 min, progressively infiltrated with LX-112 epoxy resin (Ladd Research Industries) and eventually polymerized at 60 °C for 2 days. The plastic of the plate was broken off to release resin disks with a cell monolayer on one side. Disks were cut into small pieces that were remounted for longitudinal sectioning.

To collect the mouse embryonic liver, a pregnant mouse was sacrificed and liver organs were dissected from embryos and cut into a few pieces, which were immersion fixed with 4% paraformaldehyde in 200 mM HEPES, pH 7.4, 1mM $CaCl_2$ overnight. Before resin embedding, liver tissue was cut in small pieces and additionally fixed with 1% glutaraldehyde in 200 mM HEPES, pH 7.4. Tissue was processed as described above except that epon resin was used for embedding. Tissue was sectioned at random orientation.

Serial, 90-nm thin sections were cut using a Leica Ultracut UCT ultramicrotome and deposited on formvar-coated, slot, copper grids. Sections were contrasted with 0.4% lead citrate for 1 min and imaged in a Tecnai T12 transmission electron microscope (ThermoFisher), operated at 100 kV and equipped with an axial 2k CCD camera (TVIPS).

Z-stack of images of serial sections were aligned using a TrackEM2 plugin in Fiji (Cardona et al., 2012). The liver apical membrane, bile canaliculus lumen, and junctional complex were segmented on aligned image stacks using IMOD (Kremer et al., 1996) and Blender (Blender, 2010) in order to reconstruct a 3-D model.

siRNA design, synthesis, transfection

Design of siRNA was performed using in-house software, first by testing all available sequences on the specificity for the target in mouse transcriptome (RefSeq in Pubmed), followed by elimination of sequences with significant complementarity to mouse miRNA, GC content below 25% and higher than 75% and immune responsive ones (like UGU, UGUGU, etc.). In addition, sequences were filtered using Reynolds rules (Reynolds et al., 2004). Six siRNAs with highest functionality score were selected and synthesized by solid phase phosphoramidite method, purified by IE-HPLC and verified by LC-MS (Farzan et al., 2017). Pyrimidines in the sense strand and before A in antisense strand (UA, CA dinucleotides) were 2’-O-methylated (shown by lower case letters in the sequence) and both strands were 3’-modified with phosphorothioate

bioRxiv preprint doi: https://doi.org/10.1101/2020.12.31.424978; this version posted January 1, 2021. The copyright holder for this preprint (which was not certified by peer review) is the author/funder, who has granted bioRxiv a license to display the preprint in perpetuity. It is made available under aCC-BY-NC-ND 4.0 International license.

894 dithymidylate (TsT) to enhance nuclease stability. Working stocks were prepared by diluting
895 siRNAs to 10 µM in 10 mM Tris.HCl, pH 7.5. siRNAs were transfected using transfection reagent
896 Lipofectamine™ RNAiMAX (Thermo Fisher Scientific, Cat. No. 13778075) according to the
897 reverse transfection protocol provided by the manufacturer. The final concentration per well
898 was 10 nM siRNA and 0.1 v/v% Lipofectamine™ RNAiMAX.
899
900 **Protein extraction and Western blotting**
901 Cultured cells were lysed for 20 min in ice-cold SDS lysis buffer (20 mM Tris-HCl, pH 7.5, 150
902 mM NaCl, 1 mM EDTA, 1 mM EGTA, 1% SDS, 1% NP-40 (IGEPAL CA-630), freshly added 1/1000
903 CLAAAP (Chymostatin, Leupeptin, Antipain, Aprotinin, APMSF, Pepstatin), 1/100 Phosphatase
904 Inhibitor Cocktail 2 and 3 (Sigma Aldrich). Per condition, five wells of a 96-well plate were
905 pooled together into total of 125 µl of the SDS lysis buffer. The lysates were sonicated for 3 min
906 and spun at 13000 x g for 10 min, 4°C. Protein concentration was measured with DC^{TM} Protein
907 Assay (Bio-Rad, Cat. No. 500-0116,). The samples were separated on 15% SDS-PAGE and
908 transferred onto nitrocellulose membrane. Membranes were blocked and incubated with
909 primary antibodies rabbit polyclonal anti-Rab35 (Antibody Facility MPI-CBG Dresden, F18256,
910 1:1000) and mouse monoclonal anti-γ-tubulin (Sigma-Aldrich, Cat. No. T6557, 1:2000) and
911 secondary HPR-conjugated antibodies (1:10000) in 5 % dry-milk, 10 mM Tris-HCl pH 8.0,
912 200 mM NaCl, 0.1 % Tween20. The bound antibody was detected with ECL™ Western Blotting
913 detection kit (GE Healthcare, Cat. No. RPN2209) on Hyperfilm ECL (Amersham GE Healthcare).
914 The quantification of Western blots was done with Image J (Miller, 2010), statistics were
915 calculated and plots were generated in R (R Development Core Team, 2008).
916
917 **RNA isolation and RT-qPCR**
918 Total RNA was isolated using RNeasy Mini Kit (Qiagen, Cat. No. 74104 50,) including the DNase I
919 (Qiagen, cat. No. 79254) treatment step. Cells were lysed with RTL buffer supplemented with
920 DTT. cDNA was synthesized using ProtoScript®II First Strand cDNA Synthesis Kit (NEB, Cat. No.
921 E6560S), following the manufacturer's protocol with the Random Primer Mix and the RNA
922 denaturation step. qPCR was performed on Roche LightCycler® 96 in 10-µl reactions using

bioRxiv preprint doi: https://doi.org/10.1101/2020.12.31.424978; this version posted January 1, 2021. The copyright holder for this preprint (which was not certified by peer review) is the author/funder, who has granted bioRxiv a license to display the preprint in perpetuity. It is made available under aCC-BY-NC-ND 4.0 International license.

FastStart Essential DNA Green Master (Roche, Cat. No. 06402712001). A housekeeping gene Rplp0 was used as an endogenous reference gene. Normalized relative gene expression value and % knock-down was calculated using ΔΔCq method (Haimes and Kelley, 2010), statistics were calculated and plots were generated in R (R Development Core Team, 2008).

Bulk RNA-sequencing

Two independent experiments were performed. For the experiment A following four samples were collected in 4 biological replicates: E14.5 Dlk+ hepatobalsts isolated and immediately processed for RNA isolation, *in vitro* differentiated hepatocytes from E14.5 Dlk+ hepatoblasts differentiated for 4 days in Differentiation media with 4% Matrigel grown on fibronectin coating, mature hepatocytes isolated from adult male mice following published protocols (Klingmüller et al., 2006) and immediately processed for RNA isolation. Chol/L cell line was grown as a monolayer or as a 3D cyst in 100% Matrigel drops until the polarization could be visible by proper localization of apical and lateral markers and then processed for RNA isolation. For the experiment B, the samples in 3 biological replicates were collected from *in vitro* cultured E13.5 Dlk+ hepatoblasts transfected with siRNA targeting Rab35 (siRNA #4), or non-targeting control Luciferase (siLuc) at day 5 of the culture. Rab35 mRNA knock-down was verified by RT-qPCR. The integrity of RNA was measured by Agilent 2100 Bioanalyzer. Preferentially, only samples with the RNA integrity number (RIN) > 9.0 were used. 1 µg (Experiment A) or 300 ng (Experiment B) mRNA was isolated from the total RNA by poly-dT enrichment using the NEBNext Poly(A) mRNA Magnetic Isolation Module according to the manufacturer's instructions. Final elution was done in 15ul 2x first strand cDNA synthesis buffer (NEBnext, NEB). After chemical fragmentation by incubating for 15 min at 94°C the sample was directly subjected to the workflow for strand specific RNA-Seq library preparation (Experiment A: NEBNext® Ultra™ RNA Library Prep Kit for Illumina®, Experiment B: NEBNext® Ultra™ II Directional RNA Library Prep Kit for Illumina®). For ligation custom adaptors were used (Adaptor-Oligo 1: 5'-ACA CTC TTT CCC TAC ACG ACG CTC TTC CGA TCT-3', Adaptor-Oligo 2: 5'-P-GAT CGG AAG AGC ACA CGT CTG AAC TCC AGT CAC-3'). After ligation, adapters were depleted by an XP bead purification (Beckman Coulter) adding bead in a ratio of 1:1. Indexing was done

bioRxiv preprint doi: https://doi.org/10.1101/2020.12.31.424978; this version posted January 1, 2021. The copyright holder for this preprint (which was not certified by peer review) is the author/funder, who has granted bioRxiv a license to display the preprint in perpetuity. It is made available under aCC-BY-NC-ND 4.0 International license.

during the following PCR enrichment (15 cycles, 65 °C) using custom amplification primers carrying the index sequence indicated with 'NNNNNN'. (Primer1: Oligo_Seq AAT GAT ACG GCG ACC ACC GAG ATC TAC ACT CTT TCC CTA CAC GAC GCT CTT CCG ATC T, primer2: GTG ACT GGA GTT CAG ACG TGT GCT CTT CCG ATC T, primer3: CAA GCA GAA GAC GGC ATA CGA GAT NNNNNN GTG ACT GGA GTT. After two more XP beads purifications (1:1) libraries were quantified using Qubit dsDNA HS Assay Kit (Invitrogen). For Illumina flowcell production, samples were equimolarly pooled and distributed on all lanes used for 75bp single read sequencing on Illumina HiSeq 2500 (or Illumina NextSeq 500 for the experiment B) resulting in on average 30 (or 33 for the experiment B) Mio sequenced fragments per sample.

Recombinant adenovirus production and rescue experiments

Recombinant adenovirus to express EGFP-fused Rab35 (Human RAB35 cDNA, transcript variant 1 (NM_006861.7)) was produced using AdEasy™ Vector System (Qbiogene) developed by (He et al., 1998). A linker GGGGSGGGGS was introduced between EGFP and RAB35. RAB35 fragment with the linker extension was amplified from the Addgene plasmid #47424, a gift from Peter McPherson (Allaire et al., 2010), and subcloned into pEGFP-C3 vector (Clontech) using ScaI and BamHI restriction sites. The EGFP-linker-RAB35 fragment was cloned into a transfer vector pShutle-CMV (AdEasy Vector System, Qbiogene) using SalI and HindIII restriction sites. The recombinant transfer vector was linearized by PmeI and transformed into electro-competent *E.coli* strain BJ5183-AD-1 (Stratagene, Cat. No. 200157-11) for *in vivo* recombination with pAdEasy vector. A positive clone was amplified in *E. coli* DH5α and linearized with PacI prior the transfection into the packaging cell line QBI-293A (Qbiogene HEK-293A cell derivative). Virus was amplified and purified via OptiPrep-gradient (Iodixanol 60 w/v% solution, Axis Shield, Cat. No.1114542). The control EGFP only virus was produced similarly.

E13.5 Dlk+ hepatoblasts were seeded and transfected as described above with Luc siRNA or Rab35 siRNA #4. 72h later, the cells were infected with the recombinant adenovirus (EGFP or EGFP-Rab35) at dilution 1/1000 and 1/100, respectively. The cells were cultured for 2 more days, fixed, and stained with Phalloidin-Alexa 647 and DAPI. From the acquired images, the rescue of the lumen phenotype was quantified.

bioRxiv preprint doi: https://doi.org/10.1101/2020.12.31.424978; this version posted January 1, 2021. The copyright holder for this preprint (which was not certified by peer review) is the author/funder, who has granted bioRxiv a license to display the preprint in perpetuity. It is made available under aCC-BY-NC-ND 4.0 International license.

In utero siRNA-LNP injection

For the use *in vivo*, siRNA oligos were formulated into lipid nanoparticles (LNPs) with C12-200 lipoid as previously described (Love et al., 2010). siRNA-LNPs were delivered *in utero* into E13.5 embryonic livers via vitelline vein as described elsewhere (Ahn et al., 2018). We optimized the concentration of siRNA-LNPs to 5 mg/kg body weight and the length of the treatment to 4 days using siRNAs-LNPs targeting GFP mRNA (Gilleron et al., 2013) in ROSAmG embryos (generated from the cross of ROSA mG/mT x PGKCre(J) lines). The weight of the embryos was estimated based on the published results (Kulandavelu et al., 2006). Briefly, the pregnant mice were anesthetized in a narcosis box with isoflurane at 5% then placed on a heated stage attached to a narcosis mask flowing isoflurane at 2-3%. Analgesia was ensured by injecting 4 mg/kg of Metamizol right before surgery and maintained by adding 1.33 mg/mL of the same drug in the drinking water until sacrifice. The abdomen of the mice was shaved and then sterilized with ethanol; the eyes protected from desiccation using hydration cream. The uterus was exposed via vertical laparotomy. The embryos were then injected with 5µL of LNPs at 5mg/kg. The success of the injection was assessed by blood clearance from the targeted vessel. Embryos of the same mother were randomly assigned to be non-injected, injected with control siRNA or injected with the targeting siRNA. The injections were performed using pulled needles from manually labelled glass capillaries. After injections, embryos were placed back in the abdomen and the peritoneal cavity was closed by suturing. The epidermis was then closed with surgical clips. At the end of the surgery the mice were placed close to a heating lamp and monitored until complete awakening. The livers were collected at E17.5.

Liver tissue staining with optical clearing

Embryonic livers were fixed by PFA immersion (4 % PFA, 0.1 % Tween20, PBS) for 2 hours at RT and overnight at 4 °C. The PFA was neutralized by overnight incubation in 50 mM NH_4Cl in PBS. The livers were later stored in PBS at 4 °C until processing. The livers were mounted in 4% low-melting agarose in PBS and cut into 100 µm – thick sections at a vibratome (Leica VT1200S). For deep tissue imaging, tissue sections were permeabilized with by 0.5% TtitonX100 in PBS for 1 hour at RT. The primary antibodies rat monoclonal anti-CD13 (Novus, NB100-64843, 1:500) and

bioRxiv preprint doi: https://doi.org/10.1101/2020.12.31.424978; this version posted January 1, 2021. The copyright holder for this preprint (which was not certified by peer review) is the author/funder, who has granted bioRxiv a license to display the preprint in perpetuity. It is made available under aCC-BY-NC-ND 4.0 International license.

rabbit monoclonal anti-Sox9 (Abcam, Cat. No. ab185966, 1:500) were diluted in Tx buffer (0.2% gelatin, 300 mM NaCl, 0.3% Triton X-100 in PBS) and incubated for 2 overnights at RT. After washing 5 x 15 min with 0.3% TtitonX-100 in PBS, the sections were incubated with secondary antibodies donkey anti-rat 568 (BIOTIUM, Cat. No. 20092, 1:1000), donkey anti-rabbit 647 (Thermo Fisher Scientific, Cat. No. A31573, 1:1000) and DAPI (1 mg/ml, 1:1000) and Phalloidin-Alexa488 (Thermo Fischer Scientific, Cat. No. A12379, 1:150) for another 2 overnights. After washing 5 x 15 min with 0.3% TtitonX-100 in PBS and 3 x 1 min with PBS, the optical clearing started by incubating the slices in 25% fructose for 4 hours, continued in 50% fructose for 4 hours, 75% fructose overnight, 100% fructose (100% wt/v fructose, 0.5% 1-thioglycerol, 0.1M phosphate buffer pH 7.5) for 6 hours, and finally overnight in SeeDB solution (Ke et al., 2013) (80.2% wt/wt fructose, 0.5% 1-thioglycerol, 0.1M phosphate buffer). The samples were mounted in SeeDB.

Quantification and Statistical Analysis

3D reconstruction of bile canaliculi

Optically cleared 100-µm liver sections were imaged with an upright multiphoton laser-scanning microscope (Zeiss LSM 780 NLO) equipped with Gallium arsenide phosphide (GaAsp) detectors. Liver slices were imaged twice at low (20x/0.8 Zeiss objective) and high resolution (63x/1.3 Zeiss objective, 0.3 µm voxel size), respectively. Low-resolution overviews of the complete liver sections were created and used to select for regions where enlarged apical membranes were apparent. Selected regions (~300 µm x 300 µm x 100 µm; x, y, z) were then acquired at high resolution. High-resolution images were processed and bile canaliculi segmented, based on CD13 staining, with the Motion Tracking software as described (Morales-Navarrete et al., 2015; Morales-Navarrete et al., 2016). Local lumen radius distribution was calculated by assuming a maximal radius of 10 µm.

For cells segmentation, a selected region of an image (~70 µm x 70 µm x 60 µm; x, y, z) was denoised using the PURE-LET method (Luisier et al., 2010), i.e. through the 'PureDenoise' plugin in ImageJ, with Cycle-spin = 10 and Multiframe = 11. Shading and uneven illumination were

bioRxiv preprint doi: https://doi.org/10.1101/2020.12.31.424978; this version posted January 1, 2021. The copyright holder for this preprint (which was not certified by peer review) is the author/funder, who has granted bioRxiv a license to display the preprint in perpetuity. It is made available under aCC-BY-NC-ND 4.0 International license.

then corrected using BaSiC algorithm (Peng et al., 2017) and Rolling Ball Background Subtraction plugins in Fiji, respectively. The pre-processed image was imported to Motion Tracking and apical membranes were reconstructed as above. Cells surrounding an apical tube were segmented using the 3D active mesh approach with phalloidin staining as a marker of cells border, as described in (Morales-Navarrete et al., 2015).

Lumen radius quantification

To quantify the effect of Rab35 silencing and Rab35 rescue on lumen morphology *in vitro*, a custom script was written for FIJI to segment lumina on microscopy images based on the actin signal (Phalloidin-Alexa 647) and extract region statistics. For the rescue experiment, the segmentation mask was set so that only lumina with a minimum (70%) overlap with GFP channel (expressed protein) were kept for the analysis (the cells that actually express the protein). The script contained a pause for segmentation verification and manual correction. For quantifying lumen radius, we used "local thickness" as descriptor, which can be computed with a Fiji plugin (https://imagej.net/Local_Thickness). The local thickness at any interior point of an object is defined as the diameter of the largest circle that contains the point and completely fits into the object. For each lumen, the local thickness histogram, as well as the average local thickness, was computed.

Then, the local thickness histogram of each object was normalized. To account for the different size of the objects, each normalized histogram was multiplied by a weighting factor w_i, which is proportional to the estimated volume of the object i. Without losing generality, we defined w$w_i = A_i^{3/2}$, where A_i is the number of pixels belonging to the object. Then, the histograms of all the objects in each image were summed up and normalized (i.e. to discard the effect of differences in the total amount of apical membrane between images). Finally, the averaged histograms (first over different images and then between different experiments N =3) are reported. Error bars show the standard error of the mean (SEM) per bin. The histogram quantification was performed using MATLAB R2020b.

Differential gene expression analysis

bioRxiv preprint doi: https://doi.org/10.1101/2020.12.31.424978; this version posted January 1, 2021. The copyright holder for this preprint (which was not certified by peer review) is the author/funder, who has granted bioRxiv a license to display the preprint in perpetuity. It is made available under aCC-BY-NC-ND 4.0 International license.

Basic quality control of raw sequencing data was performed with FastQC v0.11.2 (Andrews, 2010). Reads were mapped to the mouse genome reference assembly GRCm38 and genes of the Ensembl release v92 (Zerbino et al., 2018) were quantified using STAR v2.5.2b (Dobin et al., 2013). Based on the read duplication level assessed using MarkDuplicates from Picard tools v2.10.2 (Broad Institute, 2018), and dupRadar v1.8.0 (Sayols et al., 2016), the replicate 3 of the sample Chol/L cell line (3D cysts) was identified as an outlier and removed from the 'Experiment A' data set. The count data of the remaining samples were filtered for genes with more than 10 counts in any of the samples and served as input for DESeq2 v1.22.2 (Love et al., 2014) to identify differentially expressed genes using a log2fold-change threshold of 1 and an adjusted p-value cut-off of 0.01. The differential gene expression analysis of the 'Experiment B' data set was performed using DESeq2 v1.18.1 using a log2fold-change threshold of 0.5. We corrected for the batch effect due to different sample preparation days. The heatmap and the volcano plot were generated using R packages gplots (function heatmap.2) and EnhancedVolcano, respectively.

Gene Set Enrichment Analysis (GSEA)

GSEA was conducted using the tool GSEAPreranked from the software GSEA v4.1.0 (Mootha et al., 2003; Subramanian et al., 2005) with the default settings. For generating the ranked gene lists for three cell types DESeq2 1.28.1 (Love et al., 2014) was applied. The gene lists were filtered for genes with p-values < 0.05, sorted in a decreasing order by their log2FC values and used as an input for the GSEA.

Supplemental video and tables

Video Figure 1D: Formation of BC *in vitro*

Live-cell time-lapse microscopy documenting the formation of BC between two differentiating hepatoblasts expressing LifeAct-EGFP. Images acquired in 10-min intervals. Scale bar: 10 µm.

Video Figure 2F: Animation of a simplified model of BC with bulkheads

Simplified model of BC based on the 3D reconstruction in Figure 2E with periodic bulkhead-like membrane connections containing tight junctions (red) formed from the top or the bottom of

bioRxiv preprint doi: https://doi.org/10.1101/2020.12.31.424978; this version posted January 1, 2021. The copyright holder for this preprint (which was not certified by peer review) is the author/funder, who has granted bioRxiv a license to display the preprint in perpetuity. It is made available under aCC-BY-NC-ND 4.0 International license.

the lumen. The apical plasma membrane of the lumen-forming cells is represented in green and blue.

Video Figure 4B': Cysts formed upon Rab35 silencing *in vitro*

Confocal z-stack shows multiple cyst-like structures formed upon Rab35 silencing in differentiating hepatoblasts *in vitro*. Cells were stained for F-actin and nuclei. Scale bar: 30 µm.

Video Figure 5A: Formation of a spherical lumen upon Rab35 silencing *in vitro*

Live-cell time-lapse microscopy showing the growth of a spherical lumen between two differentiating hepatoblasts expressing LifeAct-EGFP upon Rab35 silencing. Images acquired in 10-min intervals. Scale bar: 10 µm.

Video Figure 5B: Formation of a multi-cellular cyst *in vitro* upon Rab35 silencing

Live-cell time-lapse microscopy documenting the formation of a multicellular cyst upon Rab35 silencing in differentiating hepatoblasts expressing LifeAct-EGFP. Images acquired in 10-min intervals. Scale bar: 10 µm.

Video Figure 7CD: 3D reconstruction of luminal network in livers injected with LNP-siLuc or LNP-siRab35

3D reconstruction of lumina labelled with an apical marker CD13 in 100 µm-thick sections of liver tissue injected with LNP-siLuc and LNP-siRab35. CD13 staining is shown first, then the 3D reconstruction based on the staining. The veins are shown in red. Scale bar: 30 µm.

Video Figure 7F: 3D reconstruction of a tubule formed in LNP-siRab35-injected liver

3D reconstruction of a tubule found in LNP-siRab35 injected livers. First, CD13 staining is shown, next, the reconstructed lumen in green, and finally reconstructed cells in random colours. The lumen is surrounded by multiple cells.

Suppl. Video S1: 3D model of BC based on EM data

3D reconstruction of EM serial sections in Figure 2B based on apical plasma membranes and tight junctions rendering. The apical plasma membrane of the lumen-forming cells is in green and blue, the tight junctions are highlighted in red.

Video Figure S1A: Formation of multiple BC lumens by a single differentiating hepatoblast

Live-cell time-lapse microscopy documenting the formation of multiple BC lumens by a single differentiating hepatoblasts expressing LifeAct-EGFP. Images acquired in 10-min intervals. Scale bar: 10 µm.

bioRxiv preprint doi: https://doi.org/10.1101/2020.12.31.424978; this version posted January 1, 2021. The copyright holder for this preprint (which was not certified by peer review) is the author/funder, who has granted bioRxiv a license to display the preprint in perpetuity. It is made available under aCC-BY-NC-ND 4.0 International license.

Video Figure S1B: Branching and fusion of BC lumen

Live-cell time-lapse microscopy of branching and fusing BC lumens formed by differentiating hepatoblasts expressing LifeAct-EGFP. Images acquired in 10-min intervals. Scale bar: 10 µm.

Video Figure S1C: Recovery of tubular BC lumen

Live-cell time-lapse microscopy documenting the adjustment of a spherical lumen into a of a tubular lumen in differentiating hepatoblasts expressing LifeAct-EGFP. Images acquired in 10-min intervals. Scale bar: 10 µm.

Table S1 (Related to Figure 4 and S4): Genes included in the focused siRNA screen

Gene name	Gene ID	Lumen phenotype	Number of siRNAs with phenotype	Category
Tjp1	21872	Loss of polarity	4/6	Apical junctions
Ocln	18260	Loss of polarity	2/6	Apical junctions
Cldn2	12738	None	0/6	Apical junctions
Gjb1	14618	None	0/6	Apical junctions
Pard3	93742	None	0/6	Apical junctions/ Cytoskeleton
Mark2 (Par1b)	13728	None	0/6	Cytoskeleton
Kif13b	16554	None	0/6	Cytoskeleton
Stk11 (Lkb1)	20869	None	0/6	Cytoskeleton
Cdc42	12540	Spherical lumina	3/6	Cytoskeleton/ Polarized trafficking
Arf6	11845	Cyst-like lumina	1/6	Cytoskeleton/ Polarized trafficking
Rab35	77407	Cyst-like lumina	5/6	Cytoskeleton/ Polarized trafficking
Rab4a	19341	None	0/6	Polarized trafficking
Rab4b	19342	None	0/6	Polarized trafficking
Rab8a	17274	None	0/6	Polarized trafficking
Rab8b	235442	None	0/6	Polarized trafficking
Rab10	19325	None	0/6	Polarized trafficking
Rab11a	53869	None	0/6	Polarized trafficking
Rab11b	19326	None	0/6	Polarized trafficking
Rab13	68328	None	0/6	Polarized trafficking
Rab14	68365	None	0/6	Polarized trafficking
Rab17	19329	None	0/6	Polarized trafficking
Rab21	216344	None	0/6	Polarized trafficking
Rab27a	11891	None	0/6	Polarized trafficking
Rab27b	80718	None	0/6	Polarized trafficking
Mal2	105853	None	0/6	Polarized trafficking

Table S2 (Related to Methods section): siRNA sequences used in the study

Excel spreadsheet

bioRxiv preprint doi: https://doi.org/10.1101/2020.12.31.424978; this version posted January 1, 2021. The copyright holder for this preprint (which was not certified by peer review) is the author/funder, who has granted bioRxiv a license to display the preprint in perpetuity. It is made available under aCC-BY-NC-ND 4.0 International license.

References

Ahn, N.J., Stratigis, J.D., Coons, B.E., Flake, A.W., Nah-Cederquist, H.D., and Peranteau, W.H. (2018). Intravenous and Intra-amniotic In Utero Transplantation in the Murine Model. J. Vis. Exp.

Akinc, A., Querbes, W., De, S., Qin, J., Frank-Kamenetsky, M., Jayaprakash, K.N., Jayaraman, M., Rajeev, K.G., Cantley, W.L., Dorkin, J.R., et al. (2010). Targeted delivery of RNAi therapeutics with endogenous and exogenous ligand-based mechanisms. Mol. Ther. *18*, 1357–1364.

Allaire, P.D., Marat, A.L., Dall'Armi, C., Di Paolo, G., McPherson, P.S., and Ritter, B. (2010). The Connecdenn DENN domain: a GEF for Rab35 mediating cargo-specific exit from early endosomes. Mol. Cell *37*, 370–382.

Andrew, D.J., and Ewald, A.J. (2010). Morphogenesis of epithelial tubes: Insights into tube formation, elongation, and elaboration. Dev. Biol. *341*, 34–55.

Andrews, S. (2010). Babraham Bioinformatics - FastQC A Quality Control tool for High Throughput Sequence Data.

Antoniou, A., Raynaud, P., Cordi, S., Zong, Y., Tronche, F., Stanger, B.Z., Jacquemin, P., Pierreux, C.E., Clotman, F., and Lemaigre, F.P. (2009). Intrahepatic Bile Ducts Develop According to a New Mode of Tubulogenesis Regulated by the Transcription Factor SOX9. Gastroenterology *136*, 2325–2333.

Berthoumieux, H., Maître, J.L., Heisenberg, C.P., Paluch, E.K., Jülicher, F., and Salbreux, G. (2014). Active elastic thin shell theory for cellular deformations. New J. Phys. *16*.

Blender, F. (2010). Blender v2.5- a 3D modeling and rendering package.

Broad Institute (2018). Picard Tools.

Bryant, D.M., and Mostov, K.E. (2008). From cells to organs: Building polarized tissue. Nat. Rev. Mol. Cell Biol. *9*, 887–901.

Cardona, A., Saalfeld, S., Schindelin, J., Arganda-Carreras, I., Preibisch, S., Longair, M., Tomancak, P., Hartenstein, V., and Douglas, R.J. (2012). TrakEM2 software for neural circuit reconstruction. PLoS One *7*.

Chaineau, M., Ioannou, M.S., and Mcpherson, P.S. (2013). Rab35: GEFs, GAPs and Effectors. Traffic *14*, 1109–1117.

Chua, C.E.L., Lim, Y.S., and Tang, B.L. (2010). Rab35 - A vesicular traffic-regulating small GTPase with actin modulating roles. FEBS Lett. *584*, 1–6.

Clark, B.S., Cui, S., Miesfeld, J.B., Klezovitch, O., Vasioukhin, V., and Link, B.A. (2012). Loss of Llgl1 in retinal neuroepithelia reveals links between apical domain size, Notch activity and neurogenesis. Development *139*, 1599–1610.

bioRxiv preprint doi: https://doi.org/10.1101/2020.12.31.424978; this version posted January 1, 2021. The copyright holder for this preprint (which was not certified by peer review) is the author/funder, who has granted bioRxiv a license to display the preprint in perpetuity. It is made available under aCC-BY-NC-ND 4.0 International license.

Cohen, D., Rodriguez-Boulan, E., and Müsch, A. (2004a). Par-1 promotes a hepatic mode of apical protein trafficking in MDCK cells. Proc. Natl. Acad. Sci. U. S. A. *101*, 13792–13797.

Cohen, D., Brennwald, P.J., Rodriguez-Boulan, E., and Müsch, A. (2004b). Mammalian PAR-1 determines epithelial lumen polarity by organizing the microtubule cytoskeleton. J. Cell Biol. *164*, 717–727.

Dambournet, D., MacHicoane, M., Chesneau, L., Sachse, M., Rocancourt, M., El Marjou, A., Formstecher, E., Salomon, R., Goud, B., and Echard, A. (2011). Rab35 GTPase and OCRL phosphatase remodel lipids and F-actin for successful cytokinesis. Nat. Cell Biol. *13*, 981–988.

Dickinson, M.E., Flenniken, A.M., Ji, X., Teboul, L., Wong, M.D., White, J.K., Meehan, T.F., Weninger, W.J., Westerberg, H., Adissu, H., et al. (2016). High-throughput discovery of novel developmental phenotypes. Nature *537*, 508–514.

Dobin, A., Davis, C.A., Schlesinger, F., Drenkow, J., Zaleski, C., Jha, S., Batut, P., Chaisson, M., and Gingeras, T.R. (2013). STAR: ultrafast universal RNA-seq aligner. Bioinformatics *29*, 15–21.

Farzan, V.M., Ulashchik, E.A., Martynenko-Makaev, Y. V., Kvach, M. V., Aparin, I.O., Brylev, V.A., Prikazchikova, T.A., Maklakova, S.Y., Majouga, A.G., Ustinov, A. V., et al. (2017). Automated Solid-Phase Click Synthesis of Oligonucleotide Conjugates: From Small Molecules to Diverse *N* -Acetylgalactosamine Clusters. Bioconjug. Chem. *28*, 2599–2607.

Fölsch, H., Ohno, H., Bonifacino, J.S., and Mellman, I. (1999). A novel clathrin adaptor complex mediates basolateral targeting in polarized epithelial cells. Cell *99*, 189–198.

Franke, C., Sauer, M., and De Linde, S. Van (2016). Photometry unlocks 3D information from 2D localization microscopy data. Nat. Methods *14*, 41–44.

Franke, C., Repnik, U., Segeletz, S., Brouilly, N., Kalaidzidis, Y., Verbavatz, J.M., and Zerial, M. (2019). Correlative single-molecule localization microscopy and electron tomography reveals endosome nanoscale domains. Traffic *20*, 601–617.

Frémont, S., Hammich, H., Bai, J., Wioland, H., Klinkert, K., Rocancourt, M., Kikuti, C., Stroebel, D., Romet-Lemonne, G., Pylypenko, O., et al. (2017). Oxidation of F-actin controls the terminal steps of cytokinesis. Nat. Commun. *8*.

Fu, D., Wakabayashi, Y., Ido, Y., Lippincott-Schwartz, J., and Arias, I.M. (2010). Regulation of bile canalicular network formation and maintenance by AMP-activated protein kinase and LKB1. J Cell Sci *123*, 3294–3302.

Fu, D., Wakabayashi, Y., Lippincott-Schwartz, J., and Arias, I.M. (2011). Bile acid stimulates hepatocyte polarization through a cAMP-Epac-MEK-LKB1-AMPK pathway. Proc. Natl. Acad. Sci. U. S. A. *108*, 1403–1408.

Gilleron, J., Querbes, W., Zeigerer, A., Borodovsky, A., Marsico, G., Schubert, U., Manygoats, K., Seifert, S., Andree, C., Stöter, M., et al. (2013). Image-based analysis of lipid nanoparticle-mediated siRNA delivery, intracellular trafficking and endosomal escape. Nat. Biotechnol. *31*,

bioRxiv preprint doi: https://doi.org/10.1101/2020.12.31.424978; this version posted January 1, 2021. The copyright holder for this preprint (which was not certified by peer review) is the author/funder, who has granted bioRxiv a license to display the preprint in perpetuity. It is made available under aCC-BY-NC-ND 4.0 International license.

638–646.

Gissen, P., and Arias, I.M. (2015). Structural and functional hepatocyte polarity and liver disease. J. Hepatol. *63*, 1023–1037.

Grosse, B., Degrouard, J., Jaillard, D., and Cassio, D. (2013). Build them up and break them down. Tissue Barriers *1*, e25210.

Haimes, J., and Kelley, M. (2010). Demonstration of a ΔΔ C q Calculation Method to Compute Relative Gene Expression from qPCR Data.

Hannezo, E., Dong, B., Recho, P., Joanny, J.F., and Hayashi, S. (2015). Cortical instability drives periodic supracellular actin pattern formation in epithelial tubes. Proc. Natl. Acad. Sci. U. S. A.

Hayashi, S., and Dong, B. (2017). Shape and geometry control of the *Drosophila* tracheal tubule. Dev. Growth Differ. *59*, 4–11.

He, T.C., Zhou, S., Da Costa, L.T., Yu, J., Kinzler, K.W., and Vogelstein, B. (1998). A simplified system for generating recombinant adenoviruses. In Proceedings of the National Academy of Sciences of the United States of America, pp. 2509–2514.

Homolya, L., Fu, D., Sengupta, P., Jarnik, M., Gillet, J.-P., Vitale-Cross, L., Gutkind, J.S., Lippincott-Schwartz, J., and Arias, I.M. (2014). LKB1/AMPK and PKA Control ABCB11 Trafficking and Polarization in Hepatocytes. PLoS One *9*, e91921.

Huch, M., Dorrell, C., Boj, S.F., Van Es, J.H., Li, V.S.W., Van De Wetering, M., Sato, T., Hamer, K., Sasaki, N., Finegold, M.J., et al. (2013). In vitro expansion of single Lgr5 + liver stem cells induced by Wnt-driven regeneration. Nature *494*, 247–250.

Jewett, C.E., and Prekeris, R. (2018). Insane in the apical membrane: Trafficking events mediating apicobasal epithelial polarity during tube morphogenesis. Traffic *19*, 666–678.

Ke, M.T., Fujimoto, S., and Imai, T. (2013). SeeDB: A simple and morphology-preserving optical clearing agent for neuronal circuit reconstruction. Nat. Neurosci. *16*, 1154–1161.

Klingmüller, U., Bauer, A., Bohl, S., Nickel, P.J., Breitkopf, K., Dooley, S., Zellmer, S., Kern, C., Merfort, I., Sparna, T., et al. (2006). Primary mouse hepatocytes for systems biology approaches: A standardized in vitro system for modelling of signal transduction pathways. IEE Proc. Syst. Biol. *153*, 433–447.

Klinkert, K., and Echard, A. (2016). Rab35 GTPase: A Central Regulator of Phosphoinositides and F-actin in Endocytic Recycling and Beyond. Traffic *17*, 1063–1077.

Klinkert, K., Rocancourt, M., Houdusse, A., and Echard, A. (2016). Rab35 GTPase couples cell division with initiation of epithelial apico-basal polarity and lumen opening. Nat. Commun. *7*, 11166.

Kouranti, I., Sachse, M., Arouche, N., Goud, B., and Echard, A. (2006). Rab35 Regulates an

bioRxiv preprint doi: https://doi.org/10.1101/2020.12.31.424978; this version posted January 1, 2021. The copyright holder for this preprint (which was not certified by peer review) is the author/funder, who has granted bioRxiv a license to display the preprint in perpetuity. It is made available under aCC-BY-NC-ND 4.0 International license.

Endocytic Recycling Pathway Essential for the Terminal Steps of Cytokinesis. Curr. Biol. *16*, 1719–1725.

Kremer, J.R., Mastronarde, D.N., and McIntosh, J.R. (1996). Computer visualization of three-dimensional image data using IMOD. J. Struct. Biol. *116*, 71–76.

Kulandavelu, S., Qu, D., Sunn, N., Mu, J., Rennie, M.Y., Whiteley, K.J., Walls, J.R., Bock, N.A., Sun, J.C.H., Covelli, A., et al. (2006). Embryonic and neonatal phenotyping of genetically engineered mice. ILAR J. *47*, 103–117.

Lallemand, Y., Luria, V., Haffner-Krausz, R., and Lonai, P. (1998). Maternally expressed PGK-Cre transgene as a tool for early and uniform activation of the Cre site-specific recombinase. Transgenic Res. *7*, 105–112.

Landau, L.D., and Lifshitz, E.M. (1986). Theory of Elasticity, Third Edition: (Course of Theoretical Physics).

Lázaro-Diéguez, F., Cohen, D., Fernandez, D., Hodgson, L., IJzendoorn, S.C.D. van, and Müsch, A. (2013). Par1b links lumen polarity with LGN–NuMA positioning for distinct epithelial cell division phenotypes. J Cell Biol *203*, 251–264.

Li, Q., Zhang, Y., Pluchon, P., Robens, J., Herr, K., Mercade, M., Thiery, J.P., Yu, H., and Viasnoff, V. (2016). Extracellular matrix scaffolding guides lumen elongation by inducing anisotropic intercellular mechanical tension. Nat. Cell Biol. *18*, 311–318.

Löf-Öhlin, Z.M., Nyeng, P., Bechard, M.E., Hess, K., Bankaitis, E., Greiner, T.U., Ameri, J., Wright, C. V., and Semb, H. (2017). EGFR signalling controls cellular fate and pancreatic organogenesis by regulating apicobasal polarity. Nat. Cell Biol. *19*, 1313–1325.

Love, K.T., Mahon, K.P., Levins, C.G., Whitehead, K.A., Querbes, W., Dorkin, J.R., Qin, J., Cantley, W., Qin, L.L., Racie, T., et al. (2010). Lipid-like materials for low-dose, in vivo gene silencing. Proc. Natl. Acad. Sci. U. S. A. *107*, 1864–1869.

Love, M.I., Huber, W., and Anders, S. (2014). Moderated estimation of fold change and dispersion for RNA-seq data with DESeq2. Genome Biol. *15*, 550.

Luisier, F., Vonesch, C., Blu, T., and Unser, M. (2010). Fast interscale wavelet denoising of Poisson-corrupted images. Signal Processing *90*, 415–427.

de Marco, M.C., Martín-Belmonte, F., Kremer, L., Albar, J.P., Correas, I., Vaerman, J.P., Marazuela, M., Byrne, J.A., and Alonso, M.A. (2002). MAL2, a novel raft protein of the MAL family, is an essential component of the machinery for transcytosis in hepatoma HepG2 cells. J. Cell Biol. *159*, 37–44.

Meyer, K., Ostrenko, O., Bourantas, G., Morales-Navarrete, H., Porat-Shliom, N., Segovia-Miranda, F., Nonaka, H., Ghaemi, A., Verbavatz, J.-M., Brusch, L., et al. (2017). A Predictive 3D Multi-Scale Model of Biliary Fluid Dynamics in the Liver Lobule. Cell Syst. *4*, 277-290.e9.

bioRxiv preprint doi: https://doi.org/10.1101/2020.12.31.424978; this version posted January 1, 2021. The copyright holder for this preprint (which was not certified by peer review) is the author/funder, who has granted bioRxiv a license to display the preprint in perpetuity. It is made available under aCC-BY-NC-ND 4.0 International license.

Meyer, K., Morales-Navarrete, H., Seifert, S., Wilsch-Braeuninger, M., Dahmen, U., Tanaka, E.M., Brusch, L., Kalaidzidis, Y., and Zerial, M. (2020). Bile canaliculi remodeling activates YAP via the actin cytoskeleton during liver regeneration . Mol. Syst. Biol. *16*.

Miller, L. (2010). Analyzing western blots with ImageJ.

Mootha, V.K., Lindgren, C.M., Eriksson, K.F., Subramanian, A., Sihag, S., Lehar, J., Puigserver, P., Carlsson, E., Ridderstråle, M., Laurila, E., et al. (2003). PGC-1α-responsive genes involved in oxidative phosphorylation are coordinately downregulated in human diabetes. Nat. Genet.

Morales-Navarrete, H., Segovia-Miranda, F., Klukowski, P., Meyer, K., Nonaka, H., Marsico, G., Chernykh, M., Kalaidzidis, A., Zerial, M., and Kalaidzidis, Y. (2015). A versatile pipeline for the multi-scale digital reconstruction and quantitative analysis of 3D tissue architecture. Elife *4*.

Morales-Navarrete, H., Nonaka, H., Segovia-Miranda, F., Zerial, M., and Kalaidzidis, Y. (2016). Automatic recognition and characterization of different non-parenchymal cells in liver tissue. In Proceedings - International Symposium on Biomedical Imaging, pp. 536–540.

Morales-Navarrete, H., Nonaka, H., Scholich, A., Segovia-Miranda, F., de Back, W., Meyer, K., Bogorad, R.L., Koteliansky, V., Brusch, L., Kalaidzidis, Y., et al. (2019). Liquid-crystal organization of liver tissue. Elife *8*.

Mrozowska, P.S., and Fukuda, M. (2016). Regulation of podocalyxin trafficking by Rab small GTPases in 2D and 3D epithelial cell cultures. J. Cell Biol. *213*, 355–369.

Müsch, A. (2014). The unique polarity phenotype of hepatocytes. Exp. Cell Res. *328*, 276–283.

Müsch, A. (2018). From a common progenitor to distinct liver epithelial phenotypes. Curr. Opin. Cell Biol. *54*, 18–23.

Muzumdar, M.D., Tasic, B., Miyamichi, K., Li, N., and Luo, L. (2007). A global double-fluorescent cre reporter mouse. Genesis *45*, 593–605.

O'Brien, L.E., Zegers, M.M.P., and Mostov, K.E. (2002). Building epithelial architecture: Insights from three-dimensional culture models. Nat. Rev. Mol. Cell Biol. *3*, 531–537.

Ober, E.A., and Lemaigre, F.P. (2018). Development of the liver: Insights into organ and tissue morphogenesis. J. Hepatol. *68*, 1049–1062.

Overeem, A.W., Bryant, D.M., and van IJzendoorn, S.C.D. (2015). Mechanisms of apical–basal axis orientation and epithelial lumen positioning. Trends Cell Biol. *25*, 476–485.

Peng, T., Thorn, K., Schroeder, T., Wang, L., Theis, F.J., Marr, C., and Navab, N. (2017). A BaSiC tool for background and shading correction of optical microscopy images. Nat. Commun. *8*.

Poncy, A., Antoniou, A., Cordi, S., Pierreux, C.E., Jacquemin, P., and Lemaigre, F.P. (2015). Transcription factors SOX4 and SOX9 cooperatively control development of bile ducts. Dev. Biol. *404*, 136–148.

bioRxiv preprint doi: https://doi.org/10.1101/2020.12.31.424978; this version posted January 1, 2021. The copyright holder for this preprint (which was not certified by peer review) is the author/funder, who has granted bioRxiv a license to display the preprint in perpetuity. It is made available under aCC-BY-NC-ND 4.0 International license.

Prior, N., Hindley, C.J., Rost, F., Meléndez, E., Lau, W.W.Y., Göttgens, B., Rulands, S., Simons, B.D., and Huch, M. (2019). Lgr5+ stem and progenitor cells reside at the apex of a heterogeneous embryonic hepatoblast pool. Dev. *146*.

R Development Core Team (2008). R: A language and environment for statistical computing.

Ramnarayanan, S.P., Cheng, C.A., Bastaki, M., and Tuma, P.L. (2007). Exogenous MAL reroutes selected hepatic apical proteins into the direct pathway in WIF-B cells. Mol. Biol. Cell *18*, 2707–2715.

Reynolds, A., Leake, D., Boese, Q., Scaringe, S., Marshall, W.S., and Khvorova, A. (2004). Rational siRNA design for RNA interference. Nat. Biotechnol. *22*, 326–330.

Riedl, J., Flynn, K.C., Raducanu, A., Gärtner, F., Beck, G., Bösl, M., Bradke, F., Massberg, S., Aszodi, A., Sixt, M., et al. (2010). Lifeact mice for studying F-actin dynamics. Nat. Methods *7*, 168–169.

Sayols, S., Scherzinger, D., and Klein, H. (2016). dupRadar: a Bioconductor package for the assessment of PCR artifacts in RNA-Seq data. BMC Bioinformatics *17*, 428.

Segal, J.M., Kent, D., Wesche, D.J., Ng, S.S., Serra, M., Oulès, B., Kar, G., Emerton, G., Blackford, S.J.I., Darmanis, S., et al. (2019). Single cell analysis of human foetal liver captures the transcriptional profile of hepatobiliary hybrid progenitors. Nat. Commun. *10*.

Senga, K., Mostov, K.E., Mitaka, T., Miyajima, A., and Tanimizu, N. (2012). Grainyhead-like 2 regulates epithelial morphogenesis by establishing functional tight junctions through the organization of a molecular network among claudin3, claudin4, and Rab25. Mol. Biol. Cell *23*, 2845–2855.

Slim, C.L., Lázaro-Diéguez, F., Bijlard, M., Toussaint, M.J.M., de Bruin, A., Du, Q., Müsch, A., and van IJzendoorn, S.C.D. (2013). Par1b Induces Asymmetric Inheritance of Plasma Membrane Domains via LGN-Dependent Mitotic Spindle Orientation in Proliferating Hepatocytes. PLoS Biol. *11*, e1001739.

Son, S., Kojima, T., Decaens, C., Yamaguchi, H., Ito, T., Imamura, M., Murata, M., Tanaka, S., Chiba, H., Hirata, K., et al. (2009). Knockdown of tight junction protein claudin-2 prevents bile canalicular formation in WIF-B9 cells. Histochem. Cell Biol. *131*, 411–424.

Subramanian, A., Tamayo, P., Mootha, V.K., Mukherjee, S., Ebert, B.L., Gillette, M.A., Paulovich, A., Pomeroy, S.L., Golub, T.R., Lander, E.S., et al. (2005). Gene set enrichment analysis: A knowledge-based approach for interpreting genome-wide expression profiles. Proc. Natl. Acad. Sci. U. S. A. *102*, 15545–15550.

Szymaniak, A.D., Mahoney, J.E., Cardoso, W.V., and Varelas, X. (2015). Crumbs3-Mediated Polarity Directs Airway Epithelial Cell Fate through the Hippo Pathway Effector Yap. Dev. Cell *34*, 283–296.

Tanimizu, N., Mitsuo Nishikawa, Hiroki Saito, Tohru Tsujimura, A.M. (2003). Isolation of

bioRxiv preprint doi: https://doi.org/10.1101/2020.12.31.424978; this version posted January 1, 2021. The copyright holder for this preprint (which was not certified by peer review) is the author/funder, who has granted bioRxiv a license to display the preprint in perpetuity. It is made available under aCC-BY-NC-ND 4.0 International license.

hepatoblasts based on the expression of Dlk/Pref-1. J. Cell Sci. *116*, 1775–1786.

Tanimizu, N., and Mitaka, T. (2016). Morphogenesis of liver epithelial cells. Hepatol. Res. *46*, 964–976.

Tanimizu, N., and Mitaka, T. (2017). Epithelial Morphogenesis during Liver Development. Cold Spring Harb. Perspect. Biol. *9*, a027862.

Tanimizu, N., Saito, H., Mostov, K., and Miyajima, A. (2004). Long-term culture of hepatic progenitors derived from mouse Dlk+ hepatoblasts. J. Cell Sci. *117*, 6425–6434.

Tanimizu, N., Miyajima, A., and Mostov, K.E. (2007). Liver progenitor cells develop cholangiocyte-type epithelial polarity in three-dimensional culture. Mol. Biol. Cell *18*, 1472–1479.

Tanimizu, N., Kaneko, K., Itoh, T., Ichinohe, N., Ishii, M., Mizuguchi, T., Hirata, K., Miyajima, A., and Mitaka, T. (2016). Intrahepatic bile ducts are developed through formation of homogeneous continuous luminal network and its dynamic rearrangement in mice. Hepatology *64*, 175–188.

Treyer, A., and Müsch, A. (2013). Hepatocyte polarity. Compr. Physiol. *3*, 243–287.

Ueno, Y., Alpini, G., Yahagi, K., Kanno, N., Moritoki, Y., Fukushima, K., Glaser, S., LeSage, G., and Shimosegawa, T. (2003). Evaluation of differential gene expression by microarray analysis in small and large cholangiocytes isolated from normal mice. Liver Int. *23*, 449–459.

Wang, T., Yanger, K., Stanger, B.Z., Cassio, D., and Bi, E. (2014). Cytokinesis defines a spatial landmark for hepatocyte polarization and apical lumen formation. J. Cell Sci. *127*, 2483–2492.

Watanabe, N., Tsukada, N., Smith, C.R., and Phillips, M.J. (1991). Motility of bile canaliculi in the living animal: Implications for bile flow.

Wolter, S., Löschberger, A., Holm, T., Aufmkolk, S., Dabauvalle, M.C., Van De Linde, S., and Sauer, M. (2012). RapidSTORM: Accurate, fast open-source software for localization microscopy. Nat. Methods *9*, 1040–1041.

Woods, A., Heslegrave, A.J., Muckett, P.J., Levene, A.P., Clements, M., Mobberley, M., Ryder, T.A., Abu-Hayyeh, S., Williamson, C., Goldin, R.D., et al. (2011). LKB1 is required for hepatic bile acid transport and canalicular membrane integrity in mice. Biochem. J. *434*, 49–60.

Yang, L., Wang, W.-H., Qiu, W.-L., Guo, Z., Bi, E., and Xu, C.-R. (2017). A single-cell transcriptomic analysis reveals precise pathways and regulatory mechanisms underlying hepatoblast differentiation. Hepatology *66*, 1387–1401.

Yuan, H., Zhang, H., Wu, X., Zhang, Z., Du, D., Zhou, W., Zhou, S., Brakebusch, C., and Chen, Z. (2009). Hepatocyte-specific deletion of Cdc42 results in delayed liver regeneration after partial hepatectomy in mice. Hepatology *49*, 240–249.

bioRxiv preprint doi: https://doi.org/10.1101/2020.12.31.424978; this version posted January 1, 2021. The copyright holder for this preprint (which was not certified by peer review) is the author/funder, who has granted bioRxiv a license to display the preprint in perpetuity. It is made available under aCC-BY-NC-ND 4.0 International license.

Zeigerer, A., Gilleron, J., Bogorad, R.L., Marsico, G., Nonaka, H., Seifert, S., Epstein-Barash, H., Kuchimanchi, S., Peng, C.G., Ruda, V.M., et al. (2012). Rab5 is necessary for the biogenesis of the endolysosomal system in vivo. Nature *485*, 465–470.

Zeigerer, A., Wuttke, A., Marsico, G., Seifert, S., Kalaidzidis, Y., and Zerial, M. (2017). Functional properties of hepatocytes in vitro are correlated with cell polarity maintenance. Exp. Cell Res. *350*, 242–252.

Zerbino, D.R., Achuthan, P., Akanni, W., Amode, M.R., Barrell, D., Bhai, J., Billis, K., Cummins, C., Gall, A., Girón, C.G., et al. (2018). Ensembl 2018. Nucleic Acids Res. *46*, D754–D761.

bioRxiv preprint doi: https://doi.org/10.1101/2020.12.31.424978; this version posted January 1, 2021. The copyright holder for this preprint (which was not certified by peer review) is the author/funder, who has granted bioRxiv a license to display the preprint in perpetuity. It is made available under aCC-BY-NC-ND 4.0 International license.

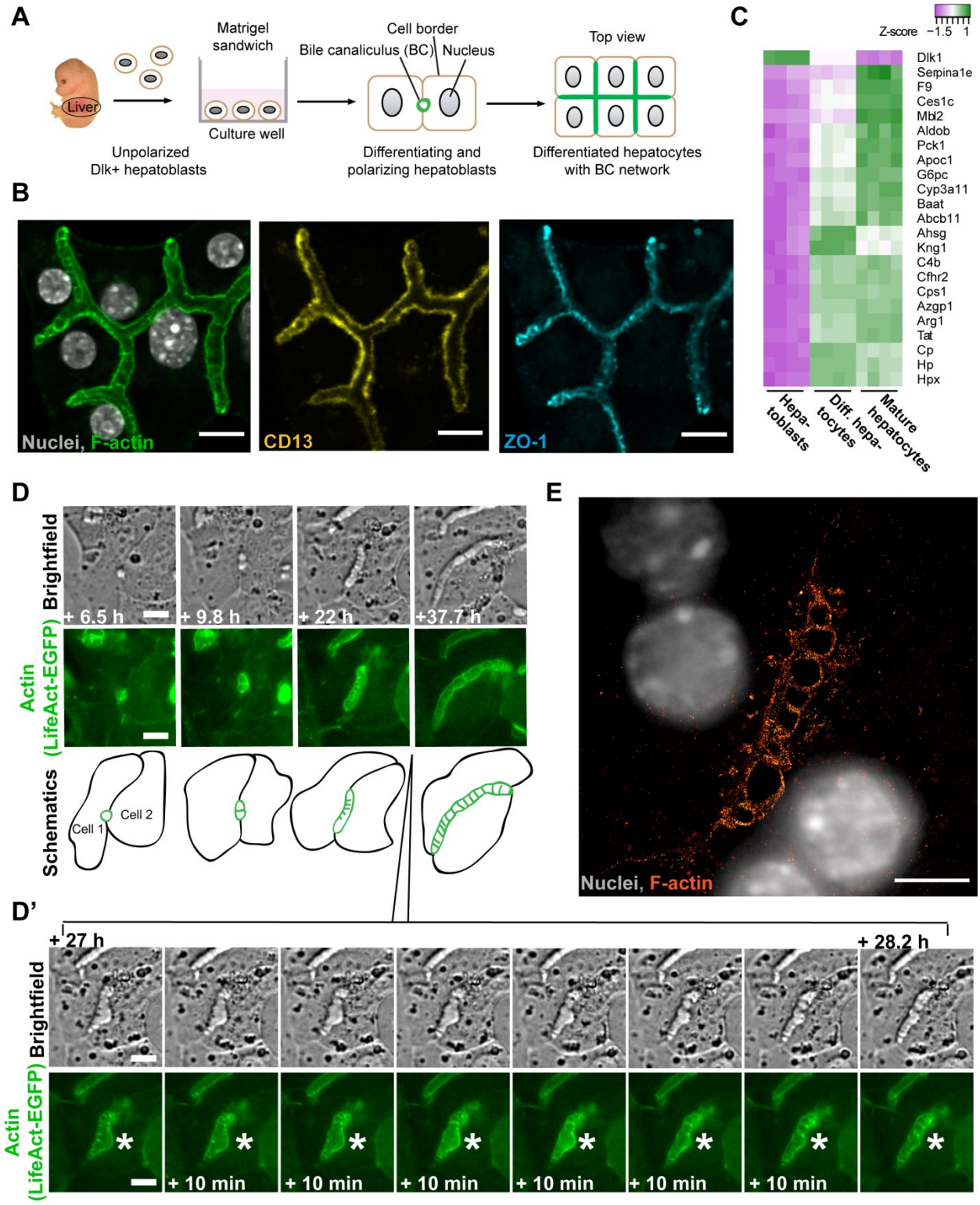

Figure 1: Lumen morphogenesis in hepatocytes is accompanied by specific actin structures that interconnect the two lumen-forming cells (See also Figure S1)

bioRxiv preprint doi: https://doi.org/10.1101/2020.12.31.424978; this version posted January 1, 2021. The copyright holder for this preprint (which was not certified by peer review) is the author/funder, who has granted bioRxiv a license to display the preprint in perpetuity. It is made available under aCC-BY-NC-ND 4.0 International license.

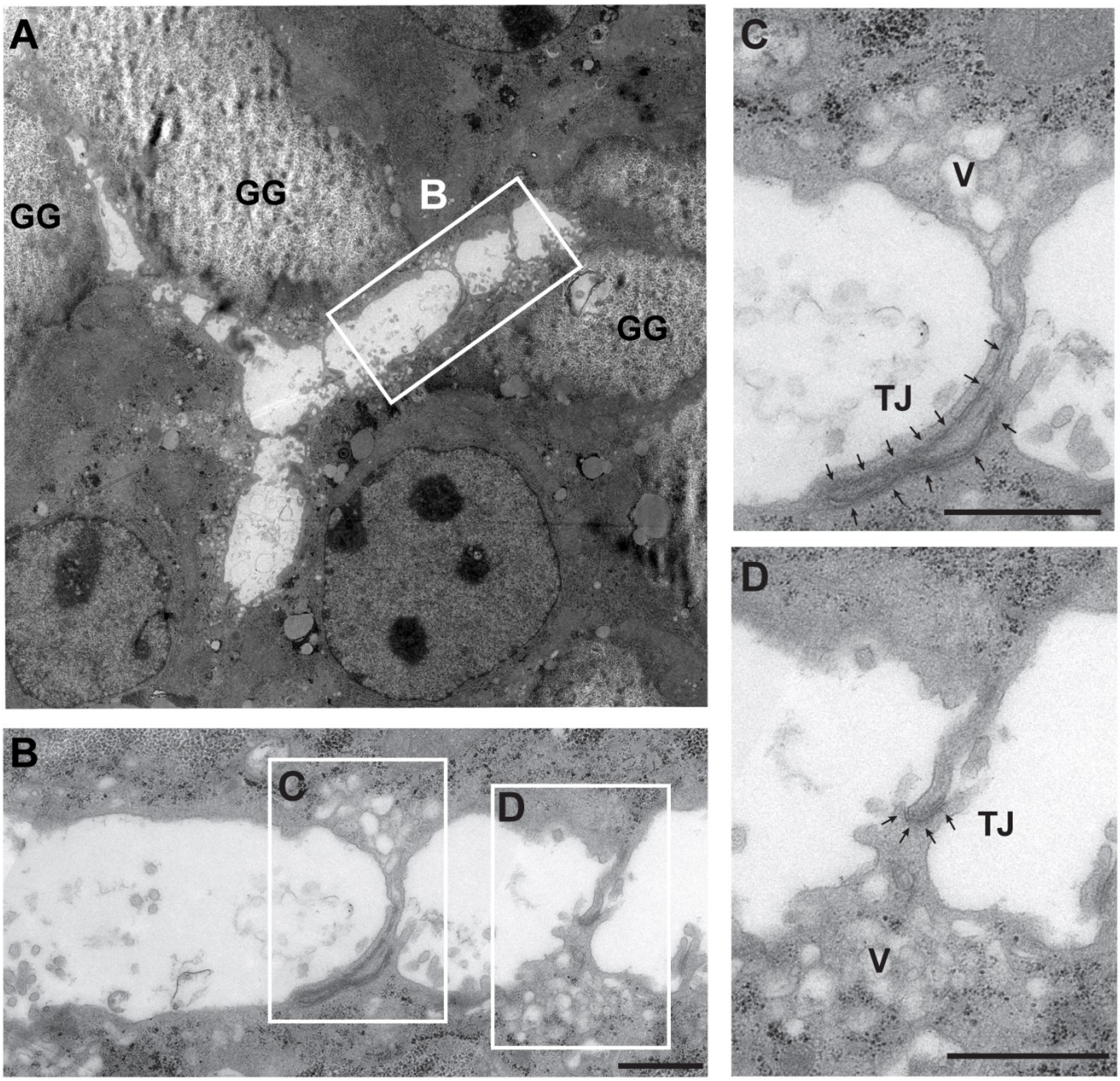

bioRxiv preprint doi: https://doi.org/10.1101/2020.12.31.424978; this version posted January 1, 2021. The copyright holder for this preprint (which was not certified by peer review) is the author/funder, who has granted bioRxiv a license to display the preprint in perpetuity. It is made available under aCC-BY-NC-ND 4.0 International license.

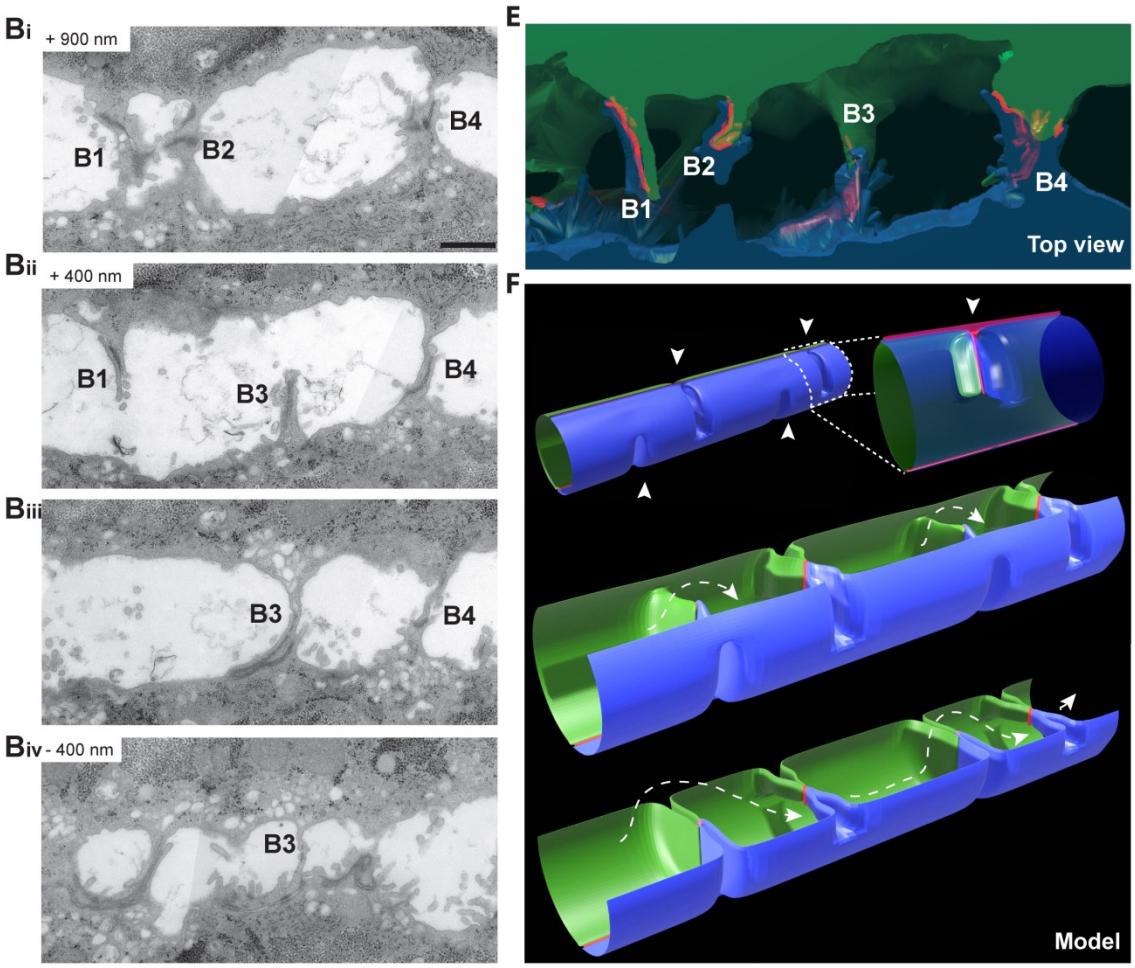

Figure 2: Ultra-structural analysis reveals a bulkhead-like pattern of transversal structures sealed by T-shaped tight junctions in the BC lumen

bioRxiv preprint doi: https://doi.org/10.1101/2020.12.31.424978; this version posted January 1, 2021. The copyright holder for this preprint (which was not certified by peer review) is the author/funder, who has granted bioRxiv a license to display the preprint in perpetuity. It is made available under aCC-BY-NC-ND 4.0 International license.

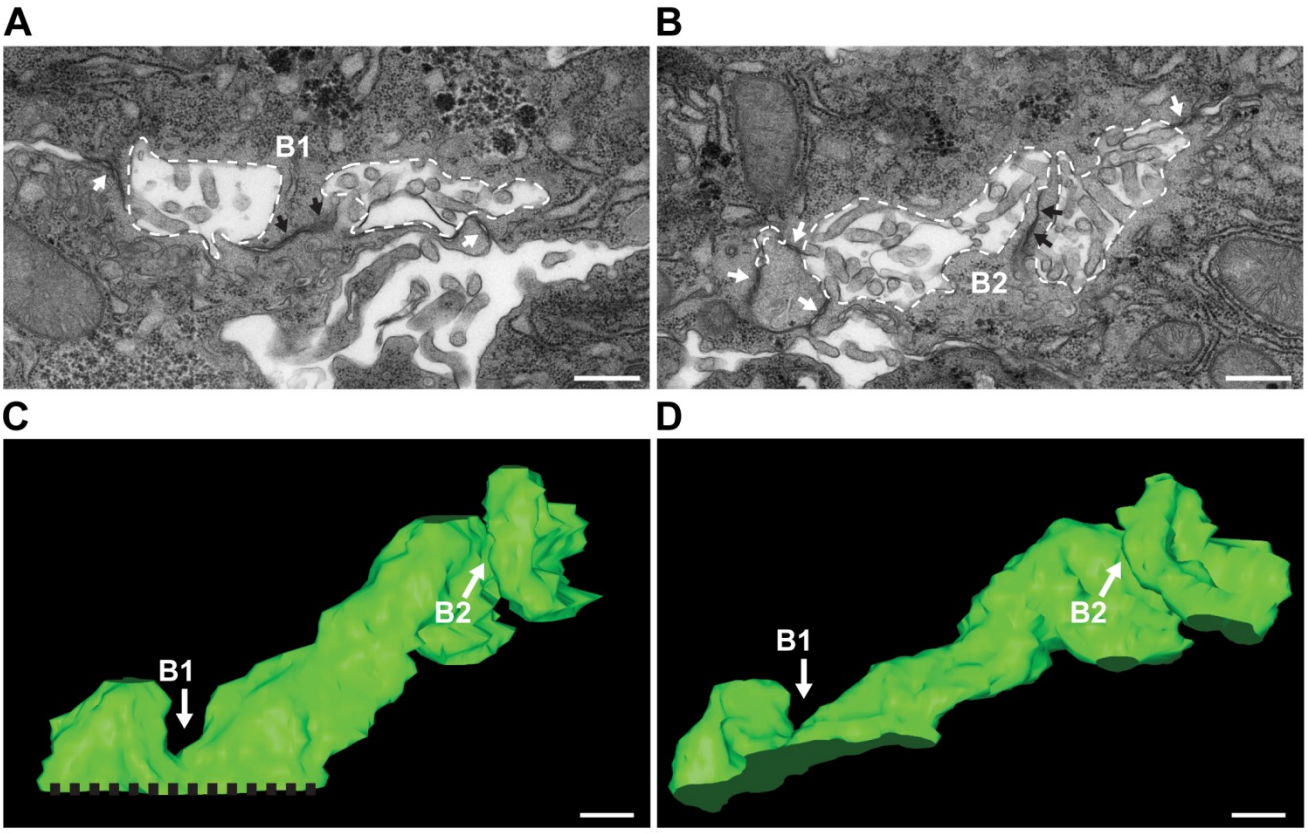

Figure 3: Transversal apical membrane structures form during BC lumen morphogenesis in embryonic liver

bioRxiv preprint doi: https://doi.org/10.1101/2020.12.31.424978; this version posted January 1, 2021. The copyright holder for this preprint (which was not certified by peer review) is the author/funder, who has granted bioRxiv a license to display the preprint in perpetuity. It is made available under aCC-BY-NC-ND 4.0 International license.

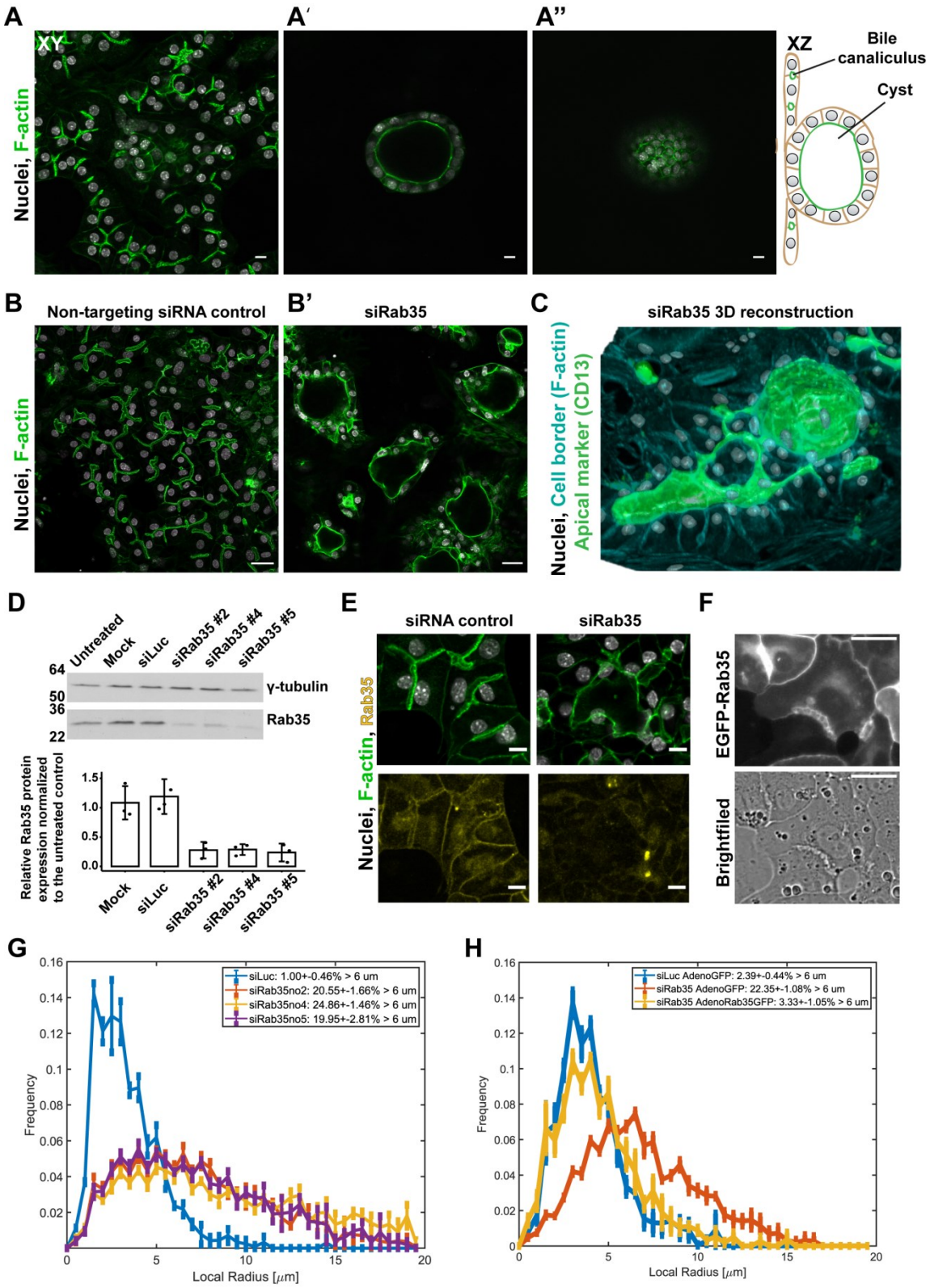

Figure 4: Conversion of hepatocyte polarity into simple apico-basal polarity (See also Figure S4)

bioRxiv preprint doi: https://doi.org/10.1101/2020.12.31.424978; this version posted January 1, 2021. The copyright holder for this preprint (which was not certified by peer review) is the author/funder, who has granted bioRxiv a license to display the preprint in perpetuity. It is made available under aCC-BY-NC-ND 4.0 International license.

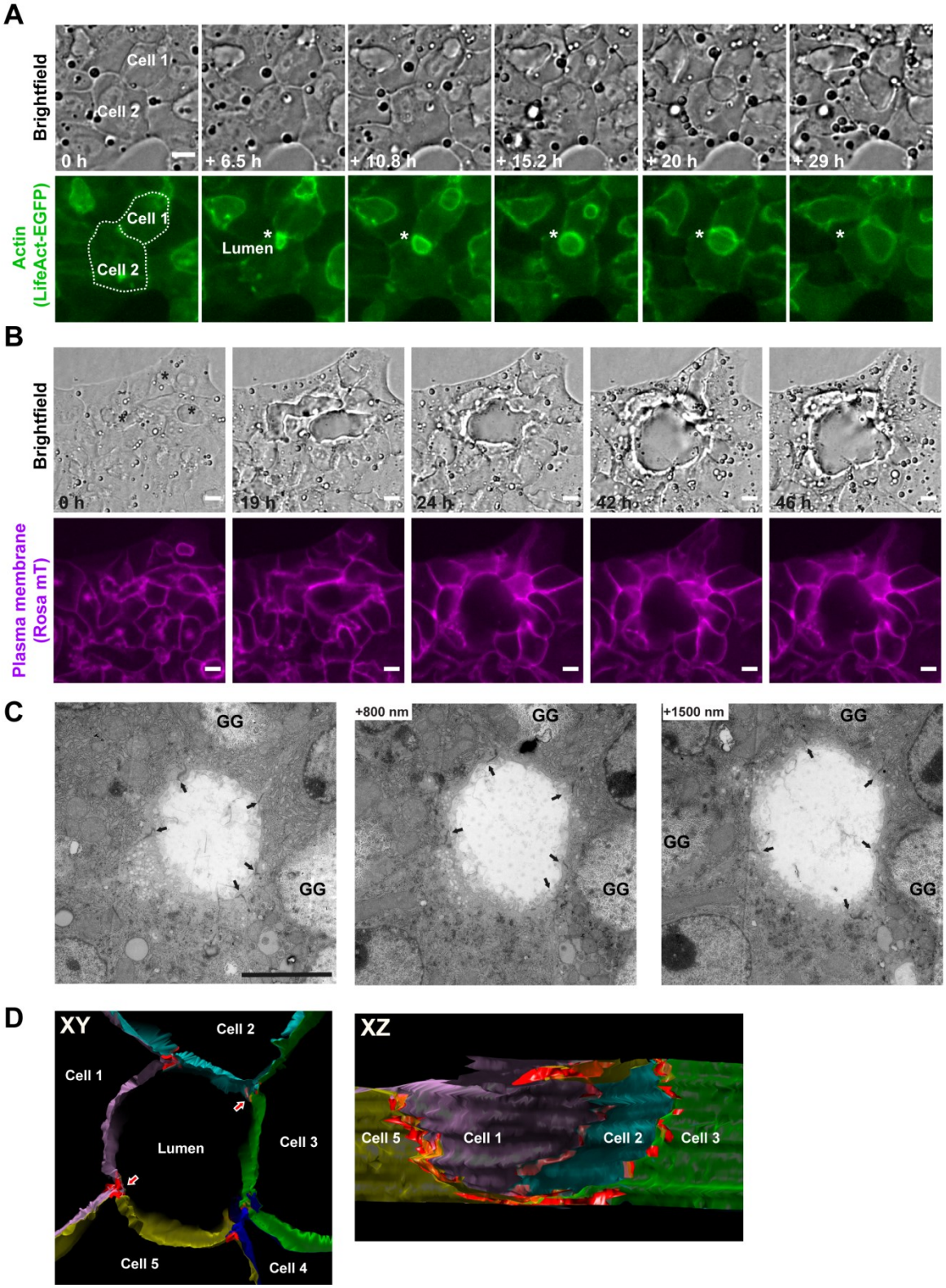

Figure 5: Silencing of Rab35 causes the loss of the transversal apical membrane bulkheads and formation of spherical cysts via a cell self-organization process

bioRxiv preprint doi: https://doi.org/10.1101/2020.12.31.424978; this version posted January 1, 2021. The copyright holder for this preprint (which was not certified by peer review) is the author/funder, who has granted bioRxiv a license to display the preprint in perpetuity. It is made available under aCC-BY-NC-ND 4.0 International license.

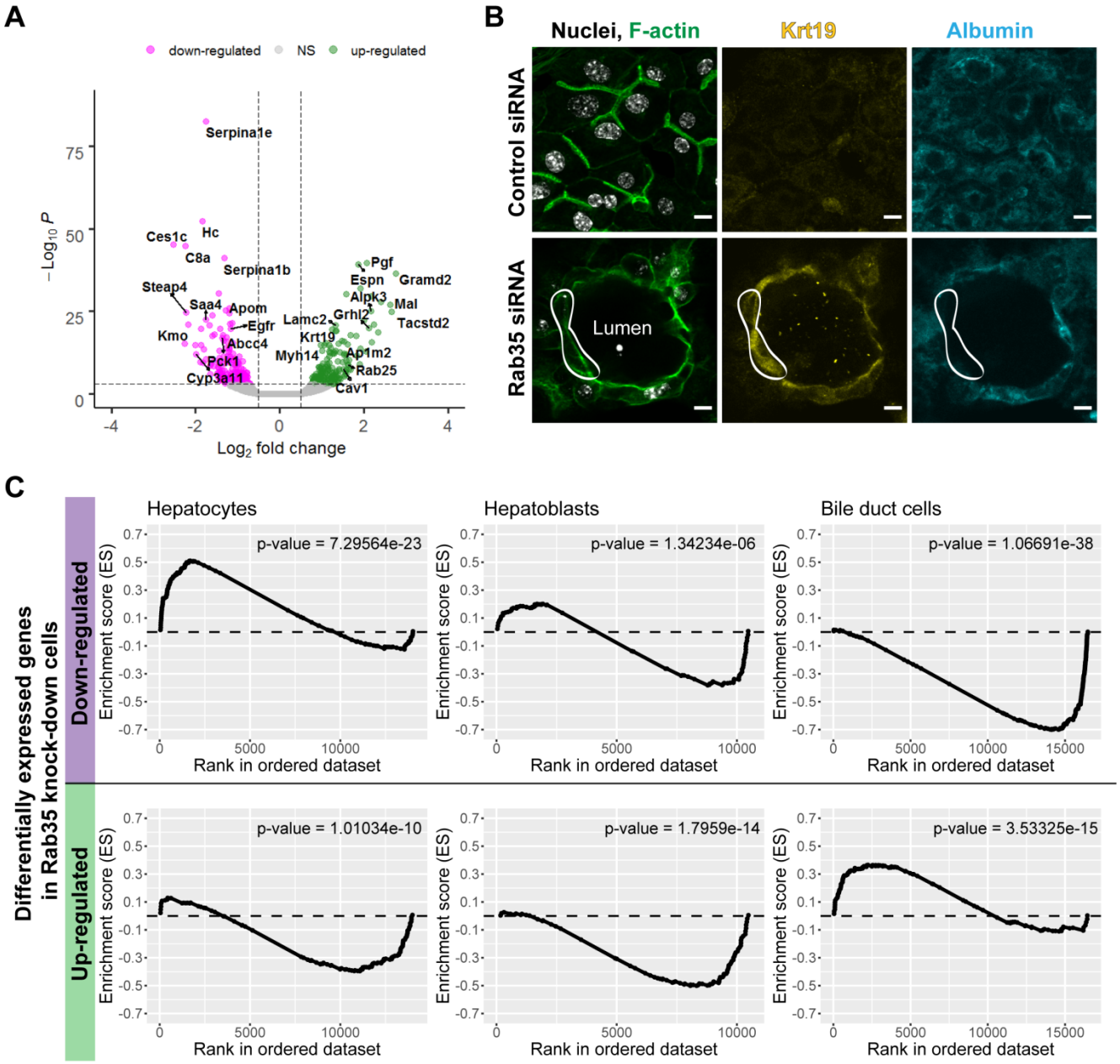

Figure 6: Down-regulation of Rab35 affects hepatocyte differentiation

bioRxiv preprint doi: https://doi.org/10.1101/2020.12.31.424978; this version posted January 1, 2021. The copyright holder for this preprint (which was not certified by peer review) is the author/funder, who has granted bioRxiv a license to display the preprint in perpetuity. It is made available under aCC-BY-NC-ND 4.0 International license.

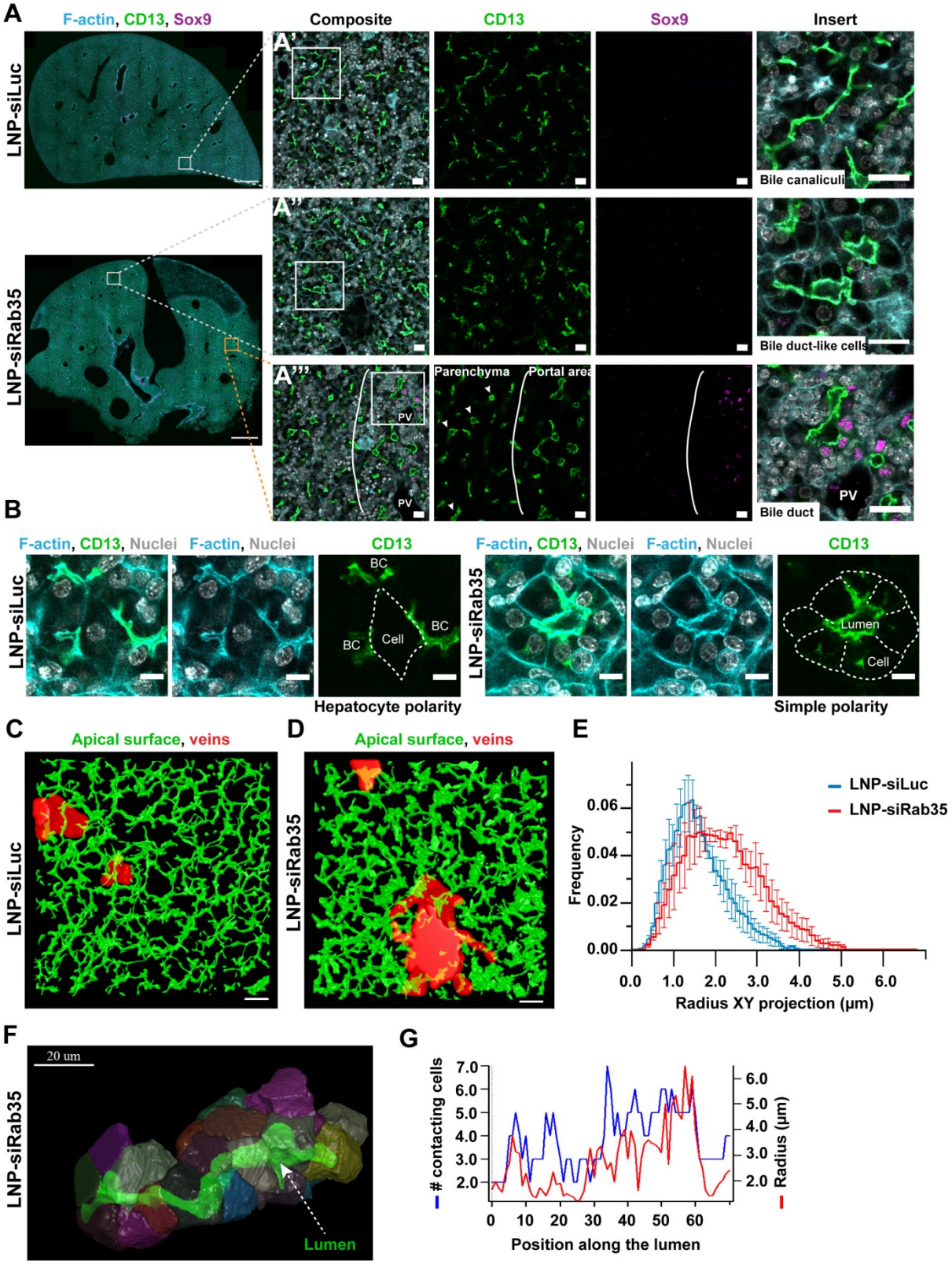

Figure 7: Silencing of Rab35 *in vivo* results in altered cell polarity and liver tissue architecture (See also Figure S7)

bioRxiv preprint doi: https://doi.org/10.1101/2020.12.31.424978; this version posted January 1, 2021. The copyright holder for this preprint (which was not certified by peer review) is the author/funder, who has granted bioRxiv a license to display the preprint in perpetuity. It is made available under aCC-BY-NC-ND 4.0 International license.

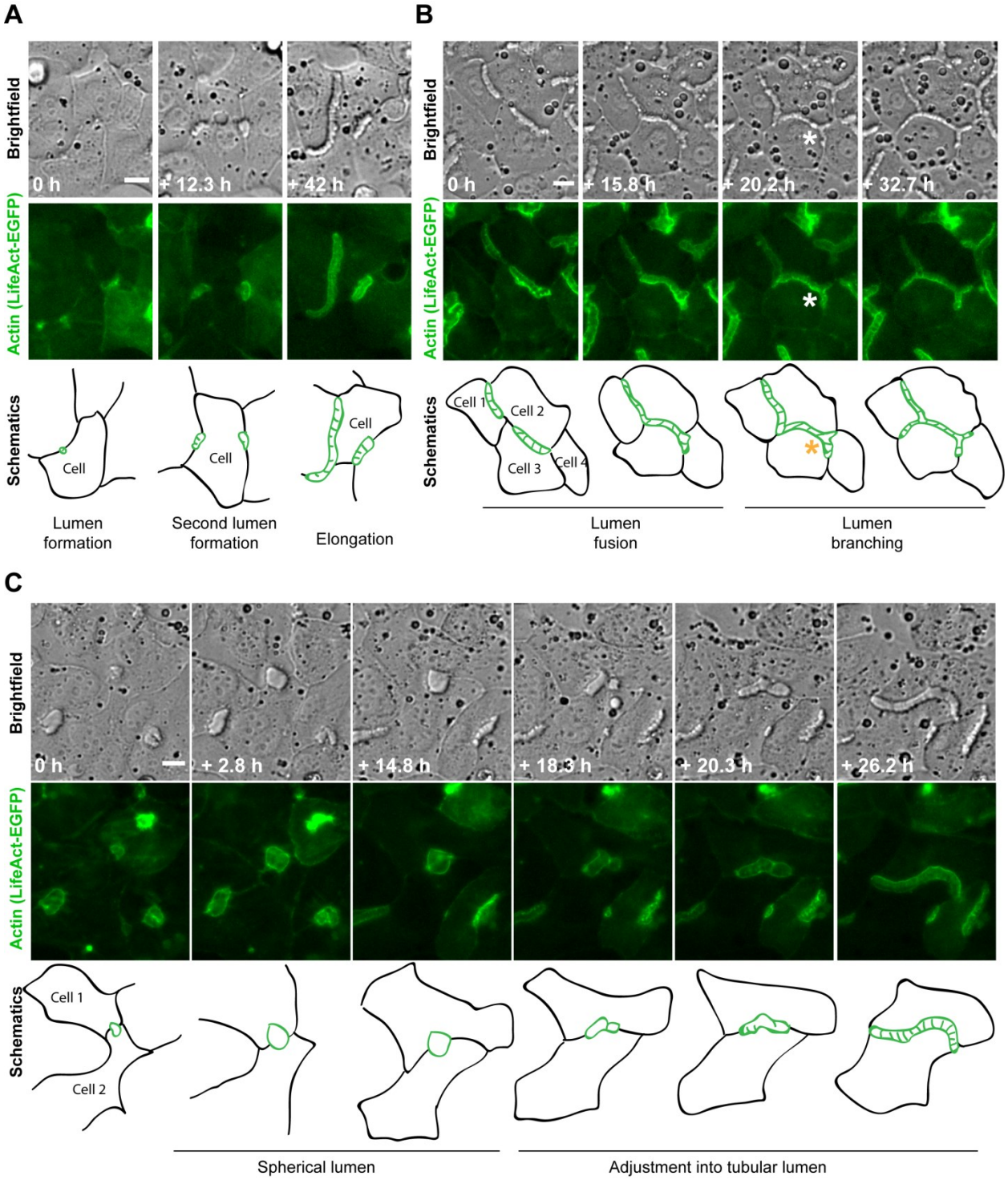

Figure S1 (Related to Figure 1): Live-cell video microscopy images of BC morphogenesis in LifeAct-EGFP expressing cells

bioRxiv preprint doi: https://doi.org/10.1101/2020.12.31.424978; this version posted January 1, 2021. The copyright holder for this preprint (which was not certified by peer review) is the author/funder, who has granted bioRxiv a license to display the preprint in perpetuity. It is made available under aCC-BY-NC-ND 4.0 International license.

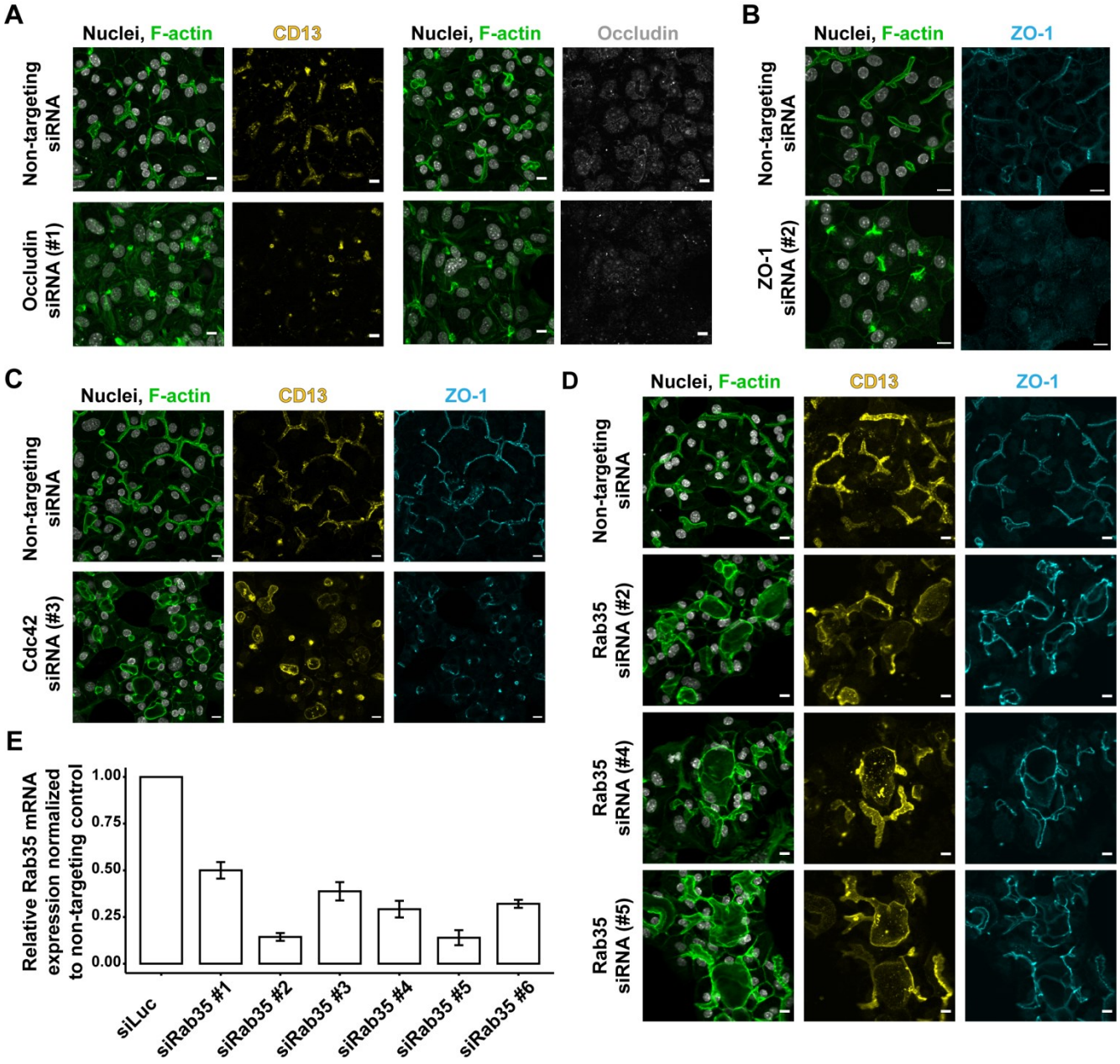

Figure S4 (Related to Figure 4): Conversion of hepatocyte polarity into simple apico-basal polarity

bioRxiv preprint doi: https://doi.org/10.1101/2020.12.31.424978; this version posted January 1, 2021. The copyright holder for this preprint (which was not certified by peer review) is the author/funder, who has granted bioRxiv a license to display the preprint in perpetuity. It is made available under aCC-BY-NC-ND 4.0 International license.

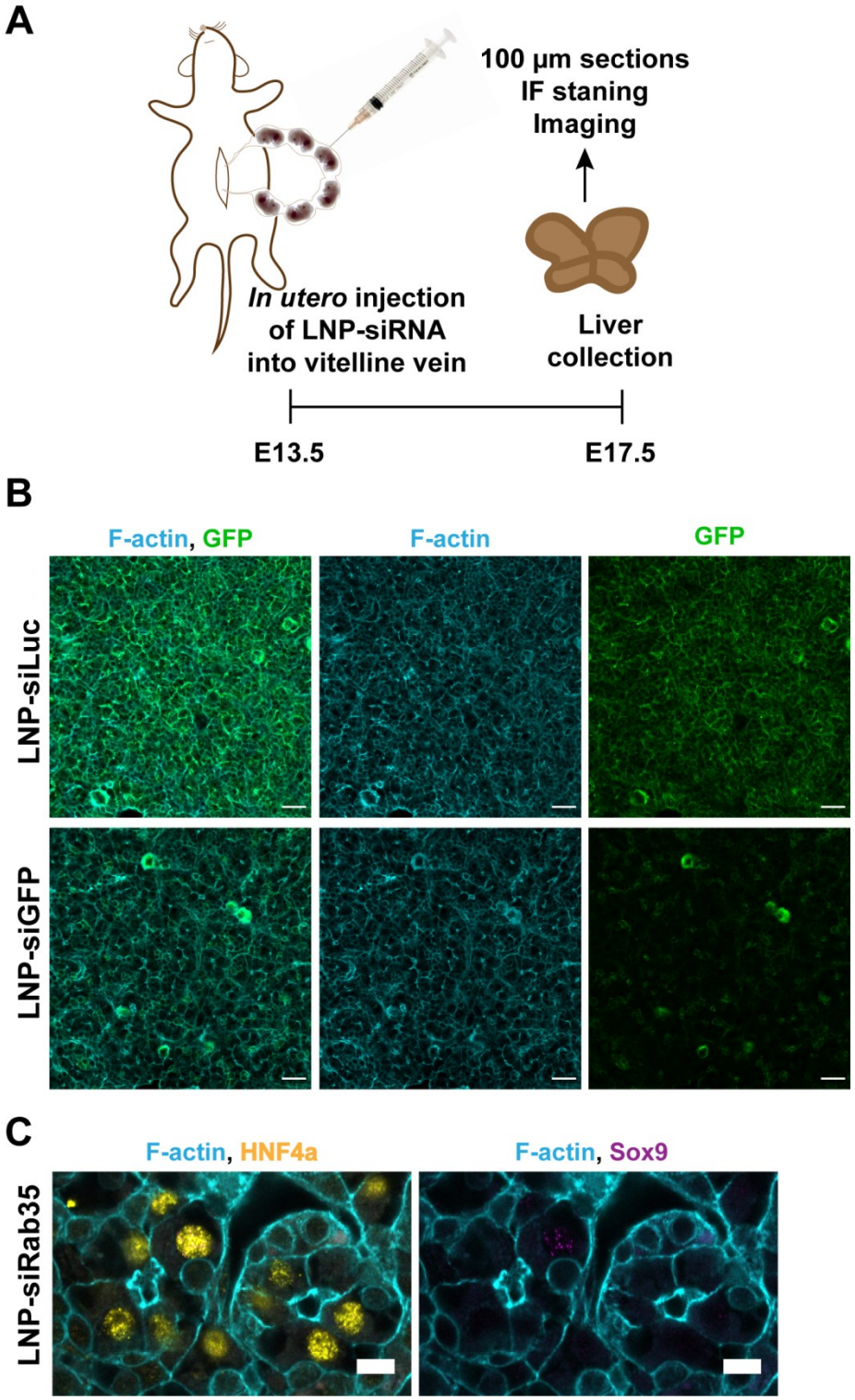

Figure S7 (Related to Figure 7): *In utero* injection method validated by silencing GFP in GFP-expressing mouse line